Magnetic anisotropic effects and electronic correlations in MnBi ferromagnet

V. P. Antropov,[1] V. N. Antonov,[1,2] L. V. Bekenov,[2] A. Kutepov,[1] and G. Kotliar[3]

[1]*Ames Laboratory USDOE, Ames, Iowa 50011, USA*
[2]*Institute of Metal Physics, 36 Vernadsky Street, 03142 Kiev, Ukraine*
[3]*Department of Physics and Astronomy, Rutgers University, Piscataway, New Jersey 08854, USA*

The electronic structure and numerous magnetic properties of MnBi magnetic systems are investigated using local spin density approximation (LSDA) with on-cite Coulomb correlations (LSDA+U) included. We show that the inclusion of Coulomb correlations provides a much better description of equilibrium magnetic moments on Mn atoms as well as the magnetic anisotropy energy behavior with temperature and magneto-optical effects. We found that the inversion of the anisotropic pairwise exchange interaction between Bi atoms is responsible for the observed spin reorientation transition at 90 K. This interaction appears as a result of strong spin orbit coupling on Bi atoms, large magnetic moments on Mn atoms, significant p-d hybridization between Mn and Bi atoms, and it depends strongly on lattice constants (anisotropic Bi-Bi exchange striction). A better agreement with the magneto-optical Kerr measurements at higher energies is obtained. We also present the detailed investigation of the Fermi surface, the de Haas–van Alphen effect, and the x-ray magnetic circular dichroism in MnBi.

I. INTRODUCTION

MnBi is an intriguing ferromagnetic material, both magnetically and structurally. Manganese alloys usually tend to exhibit antiferromagnetic order, because they have nearly half-filled 3d bands, but MnBi is one of the few known ferromagnetic manganese compounds which can be used as a permanent magnet [1]. Its other interesting magnetic properties include an extraordinarily large Kerr rotation [2], with a Curie temperature above room temperature (RT) [3], a large perpendicular anisotropy in thin films at RT [4], and a high coercivity that increases with temperature [5]. The low-temperature phase (LTP) of MnBi is ferromagnetic and has the hexagonal NiAs structure. With increasing temperature, the material remains ferromagnetic up to 628 K and then undergoes a coupled structural and magnetic phase transition to a paramagnetic high-temperature phase (HTP). The HTP is a disordered NiAs phase where 10%–15% of the large bipyramidal interstitial sites are occupied by Mn atoms [6]. Rapid cooling of HTP MnBi yields a quenched high-temperature phase, which is also ferromagnetic with even larger uniaxial magnetocrystalline anisotropy energy (MAE), but smaller magnetization and Curie temperature.

At RT MnBi is known to have an extremely high MAE ($K \sim 107$ ergs/cm^3). This decreases rapidly, however, with decreasing temperature and vanishes at $\sim$90 K (T_{SR}) [7]. The experiments indicated the presence of a spin-reorientation transition during this temperature decrease [5]. Among known hard magnetic materials, MnBi is one of few alloys where the coercive field increases with increasing temperature, reflecting the magnetic anisotropy trend.

Historically, the ferromagnetic nature of manganese-bismuth alloys was first reported by Heusler around 1904 [8]. In 1914 Bekier considered the formation of a phase MnBi as probable; the phase results from a peritectic reaction at 450 °C between pure manganese and the melted alloy containing 9% of manganese [9]. Parravano and Perret [10] established the phase diagram for this system and isolated crystals containing 19.9% manganese, which they considered

to be the MnBi phase. Hilpert and Dieckmann [11] noted the strong ferromagnetism of these alloys and placed the Curie temperature at around 360–380 °C. Furst and Halla later concluded from x-ray studies that a single compound was present with the structure Mn$_2$Bi [12]. Montignie, however, showed that MnBi represented the only stable compound [13]. In further studies by Halla and Montignie, the same results were obtained [14].

The most comprehensive studies of this material were performed by Guillaud in 1943 in Strasbourg. As a part of his Ph.D. thesis, he was the first to prepare the hexagonal MnBi compound and study its numerous magnetic properties [15]. In addition to measuring the saturation moment, MAE, and Curie temperature, he established the dependence of the high coercive force of MnBi on its magnetic anisotropy and reduced particle size. He also was first to observe the spin reorientation and a corresponding increase of magnetic anisotropy with temperature. Because of these considerations, around 60 years ago, MnBi was chosen for investigation by the U.S. Naval Ordnance Laboratory. As a result, a new permanent magnetic alloy "bismanol" was developed [16]. Bismanol has very high coercive force and moderate energy density, making it a good choice for small electric motors. However, due to oxidation and corrosion problems, bismanol has not been used much as a practical magnet.

Nevertheless, studies of both fundamental and applied properties relevant for permanent magnetism have never been abandoned and this material attracted the attention of a new generation of researchers. Hihara and Köi [17] studied the temperature dependence of the easy axis of the magnetization in MnBi using the nuclear magnetic resonance method. They found that for high temperatures above 142 K, the easy axis of magnetization is along the c direction. As the temperature is decreased between the $T_{SR1} = 142$ K and $T_{SR} = 90$ K (spin canting interval), the polar angle θ gradually deviates from the c axis to $\theta_{\text{exper}} \sim 37°$. The magnetization flops into the ab basal plane at 90 K. This spin reorientation was also observed by neutron diffraction [5,7] and magnetization measurements on MnBi single crystals [18]. To our knowledge, no theoretical

explanation of all these observed effects has been proposed in literature.

Nearly simultaneously with bismanol's development, MnBi became the subject of another research activity after being recognized that, in the form of thin films, it had quite favorable properties with regard to potential applications for magneto-optical (MO) recording [19–22] (see references prior to 1988 and discussion in Ref. [23]). The MO properties of MnBi were measured by several authors [2,24–26]. The most extensive study was carried out by Di *et al.* [2,25]. Their measured Kerr angle spectrum for MnBi has peaks at 1.84 and 3.35 eV. The former have a relatively large magnitude of 2.31° at 85 K.

The electronic band structure of MnBi has been calculated by several authors [5,27–44]. The optical and MO spectra of MnBi have been calculated in Refs. [29,30,32,33,35]. However, there are still disagreements about the interpretation of the MO spectra. The major disagreement concerns the lack of theoretical description of a high energy peak of the Kerr rotation observed experimentally at 3.35 eV.

Köhler and Kübler [32,33] obtained only one peak at 1.8 eV. They hypothesized that the thin-film samples may have considerable impurities from materials in contact with them. They found that oxygen, as an impurity, produced a second peak, but energies of both peaks were not in good agreement with the experiment. Ravindran *et al.* [35], on the other hand, did find a second peak in their calculated Kerr-angle spectrum for pure MnBi. Oppeneer *et al.* [30] obtained a large negative peak at 1.8 eV. This is in agreement with experiment. They then found only a shoulder around 3.4 eV. Here, the experimental data has a pronounced peak. Since the data of Di *et al.* [2,25] were taken on a sample with the composition Mn$_{1.22}$Bi, Oppeneer *et al.* [30] simulated this material and found a calculated Kerr-angle spectrum with a similar but weaker peak at 1.8 eV and a second peak at 4.3 eV. This is higher in energy than that for MnBi. All previous studies of MO properties of MnBi were performed in the local spin density approximation (LSDA) approximation and value of magnetic moment was significantly underestimated.

Below we provide a theoretical explanation for the long-standing experimental puzzles in the measured MO properties, magnetic anisotropy and spin orientation. We show that all the physical properties under consideration can be properly described only taking into account spin-orbit (SO) interaction and a proper strength of Coulomb electron-electron correlations.

The paper is organized as follows. The crystal structure of MnBi and computational details are presented in Sec. II. Section III presents results and discussions of electronic and magnetic structures, magnetic moments, Fermi surface (FS), orbital dependence of the cyclotron masses, extremal cross sections of the FS, MO Kerr spectra, x-ray magnetic circular dichroism, and temperature dependence of the MAE of MnBi. The results are summarized in Sec. IV.

II. CRYSTAL STRUCTURE AND CALCULATION DETAILS

A. Crystal structure

Figure 1 depicts the crystal and magnetic structure of MnBi. It exhibits large trigonal-bipyramidal interstitial sites, which
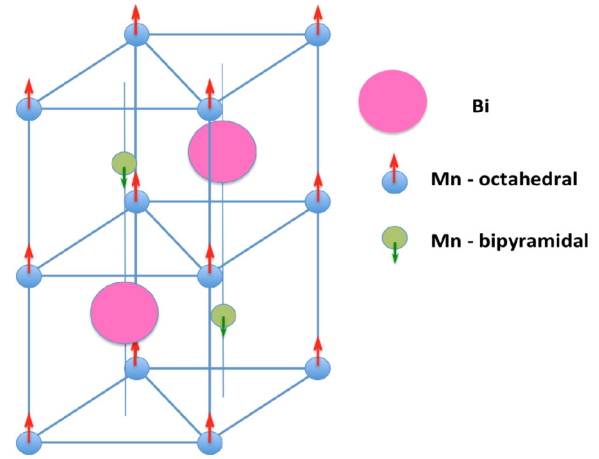

FIG. 1. (Color online) Crystal lattice of MnBi LTP phase.

may be occupied by dopant or Mn atoms. It is speculated that octahedral Mn atoms are ferromagnetically coupled with the spin parallel to the c axis, and the bipyramidal Mn atoms are antiferromagnetically coupled to the octahedral Mn atoms and result in reduced net magnetization [7,45].

The LTP phase of MnBi is ferromagnetic and has a hexagonal NiAs-type structure with unit cell dimensions $a = 4.29$ Å, $c = 6.13$ Å. On heating above $360\,°$C (T_t) there is a first order phase transition to a paramagnetic [3] state (HTP). The MnBi compounds in the LTP phase have the NiAs structure ($P6\bar{3}/mmc$ symmetry, group number 194). The unit cell consists of two Mn atoms at the Wyckoff 2a sites $(0, 0, 0)$ and $(0, 0, \frac{1}{2})$ and two Bi atoms at the Wyckoff 2c sites $(\frac{1}{3}, \frac{2}{3}, \frac{1}{4})$ and $(\frac{2}{3}, \frac{1}{3}, \frac{3}{4})$.

B. Calculation details

(a) Magneto-optical properties and x-ray magnetic circular dichroism. For the polar Kerr magnetization geometry and a crystal of tetragonal symmetry, where both the fourfold axis and the magnetization **M** are perpendicular to the sample surface and the z axis is chosen to be parallel to them, the dielectric tensor is composed of the diagonal ε_{xx} and ε_{zz}, and the off-diagonal ε_{xy} components in the form

$$\boldsymbol{\varepsilon} = \begin{pmatrix} \varepsilon_{xx} & \varepsilon_{xy} & 0 \\ -\varepsilon_{xy} & \varepsilon_{xx} & 0 \\ 0 & 0 & \varepsilon_{zz} \end{pmatrix}. \tag{1}$$

The various elements $\hat{\varepsilon}_{\alpha\beta}$ are composed of real and imaginary parts as follows: $\hat{\varepsilon}_{\alpha\beta} = \varepsilon_{\alpha\beta}^{(1)} + i\varepsilon_{\alpha\beta}^{(2)}$, where $\alpha,\beta \equiv x,y,z$, $\varepsilon_{xx} = (n + ik)^2$, and n and k are refractive index and extinction coefficient, respectively. The optical conductivity tensor $\hat{\sigma}_{\alpha\beta} = \sigma_{\alpha\beta}^{(1)} + i\sigma_{\alpha\beta}^{(2)}$ is related to the dielectric tensor $\varepsilon_{\alpha\beta}$ through the equation

$$\hat{\varepsilon}_{\alpha\beta}(\omega) = \delta_{\alpha\beta} + \frac{4\pi i}{\omega}\hat{\sigma}_{\alpha\beta}(\omega). \tag{2}$$

The Kerr rotation θ and ellipticity η are expressed as follows [46]:

$$\theta + i\eta \approx \frac{-\varepsilon_{xy}}{(\varepsilon_{xx} - 1)\sqrt{\varepsilon_{xx}}}. \tag{3}$$

The optical conductivity of MnBi has been computed from the energy band structure by means of the Kubo-Greenwood [47] linear-response expression [48]:

$$\sigma_{\alpha\beta}(\omega) = \frac{-ie^2}{m^2\hbar V_{uc}}$$
$$\times \sum_{\mathbf{k}} \sum_{nn'} \frac{f(\epsilon_{n\mathbf{k}}) - f(\epsilon_{n'\mathbf{k}})}{\omega_{nn'}(\mathbf{k})} \frac{\Pi_{n'n}^{\alpha}(\mathbf{k})\Pi_{nn'}^{\beta}(\mathbf{k})}{\omega - \omega_{nn'}(\mathbf{k}) + i\gamma}, \tag{4}$$

where $f(\epsilon_{n\mathbf{k}})$ is the Fermi function, $\hbar\omega_{nn'}(\mathbf{k}) \equiv \epsilon_{n\mathbf{k}} - \epsilon_{n'\mathbf{k}}$ is the energy difference of the Kohn-Sham energies $\epsilon_{n\mathbf{k}}$, and γ is the lifetime parameter; it is included to describe the finite lifetime of the excited Bloch electron states. The $\Pi_{nn'}^{\alpha}$ are the dipole optical transition matrix elements. In a fully relativistic description, these are given by

$$\mathbf{\Pi}_{nn'}(\mathbf{k}) = \langle \psi_{n\mathbf{k}} | c\boldsymbol{\alpha} | \psi_{n'\mathbf{k}} \rangle \tag{5}$$

with the four-component Bloch electron wave function $\psi_{n\mathbf{k}}$, velocity of light c, and Dirac operator $\boldsymbol{\alpha}$. The combined correction terms were also taken into account in the optical matrix element calculations. A detailed description of the optical matrix elements in the Dirac representation is given in Refs. [49,50].

Within the one-particle approximation, the absorption coefficient $\mu_j^{\lambda}(\omega)$ for incident x ray of polarization λ and photon energy $\hbar\omega$ can be determined as the probability of electronic transitions from initial core states with the total angular momentum j to final unoccupied Bloch states

$$\mu_{\lambda}^j(\omega) = \sum_{m_j} \sum_{n\mathbf{k}} |\langle \Psi_{n\mathbf{k}} | \Pi_{\lambda} | \Psi_{jm_j} \rangle|^2 \delta(E_{n\mathbf{k}} - E_{jm_j} - \hbar\omega)$$
$$\times \theta(E_{n\mathbf{k}} - E_F), \tag{6}$$

where Ψ_{jm_j} and E_{jm_j} are the wave function and the energy of a core state with the projection of the total angular momentum m_j; $\Psi_{n\mathbf{k}}$ and $E_{n\mathbf{k}}$ are the wave function and the energy of a valence state in the nth band with the wave vector $\mathbf{k}$; E_F is the Fermi energy. $\Pi_{\lambda} = -e\boldsymbol{\alpha}\mathbf{a}_{\lambda}$ is the electron-photon interaction operator in the dipole approximation (5), $\mathbf{a}_{\lambda}$ is the λ polarization unit vector of the photon vector potential, with $a_{\pm} = 1/\sqrt{2}(1,\pm i,0)$, $a_{\parallel} = (0,0,1)$. Here, $+$ and $-$ denotes, respectively, left and right circular photon polarizations with respect to the magnetization direction in the solid. X-ray magnetic circular and linear dichroism are given then by $(\mu_+ - \mu_-)$ and $[\mu_{\parallel} - (\mu_+ + \mu_-)/2]$, respectively.

Usually, the exchange splitting of a core shell is small compared to the bandwidth of final valence states and can be neglected. However, the exchange splitting of the $2p_{1/2,3/2}$ states of $3d$ transition metals may be as large as 0.4 eV. Then, transitions from core states with different m_j in Eq. (6) occur at different photon frequencies. This may lead to the appearance of giant x-ray magnetic linear dichroism in cubic $3d$ metals and its strong dependence on the magnetization direction [51].

At the core level, x-ray magnetic circular dichroism (XMCD) is not only element specific but also orbital specific. For $3d$ transition metals, the electronic states can be probed by the K, $L_{2,3}$, and $M_{2,3}$ x-ray absorption and emission spectra. In Bi, one can use the K, $L_{2,3}$, $M_{2,3}$, $M_{4,5}$, $N_{2,3}$, $N_{4,5}$, $N_{6,7}$, and $O_{2,3}$ spectra. For unpolarized absorption spectra $\mu^0(\omega)$ allows only transitions with $\Delta l = \pm 1$, $\Delta j = 0, \pm 1$ (dipole selection rules). Therefore only electronic states with an appropriate symmetry contribute to the absorption and emission spectra under consideration.

(b) Magnetocrystalline anisotropy. The internal energy of ferromagnetic materials depends on the direction of spontaneous magnetization. Here we consider one part of this energy, the MAE, which possesses the crystal symmetry of the material. For the material exhibiting uniaxial anisotropy, such as a hexagonal crystal, the MAE can be expressed as [52]

$$K = K_1 \sin^2\theta + K_2\sin^4\theta + K_3'\sin^6\theta$$
$$+ K_3 \sin^2\theta \, \cos[6(\phi + \psi)] + \cdots, \tag{7}$$

where K_i is the anisotropy constant of the ith order, θ and ϕ are the polar angles of the Cartesian coordinate system where the c axis coincides with the z axis (the Cartesian coordinate system was chosen such that the x axis is rotated through $90°$ from the hexagonal axis) and ψ is the phase angle.

Here, we study MAE caused only by the SO interaction and define it as the difference between two self-consistently calculated and fully relativistic total energies for two different magnetic field directions, $K = E(\theta) - E(\langle 0001 \rangle)$.

(c) Calculation details. The calculations presented in this work were performed using the spin-polarized fully relativistic LMTO method [53] (denoted further as LSDA+SO). To understand the influence of the SO interaction on the MO properties and MAE, we used the scalar relativistic magnetic Hamiltonian with SO coupling added variationally [54]. The basis consisted of s, p, d, and f LMTOs. While our fully relativistic treatment still has some approximations of the second order over $1/c$ [55], it has more complete basis set due to presence of both the large and small components of the Dirac wave function. The **k**-space integration was performed with an improved tetrahedron method [56]. To attain good convergence in total energy, a large number of **k** points has to be used in the calculations. To resolve the difference in total energies and to investigate the convergence, we used 12 008 and 18 986 **k** points in the irreducible part of the Brillouin zone. This corresponds to 46 656 and 74 088 **k** points in full zone.

(d) Treatment of the Coulomb correlations. It is well known that the LSDA fails to describe the electronic structure and properties of the systems in which the interaction among the electrons is strong. In recent years, more advanced methods of electronic structure determination such as LSDA plus self-interaction corrections [57], the LSDA+U [58] method, GW approximation [59,60], and dynamical mean-field theory [61,62] have sought to remedy this problem and have shown considerable success. Among them, the LSDA+U method is the simplest and most frequently used. We used the "relativistic" generalization of the rotationally invariant version of the LSDA+U method [63] which takes into

account SO coupling so that the occupation matrix of localized electrons becomes nondiagonal in spin indexes.

The screened Coulomb U and exchange J integrals enter the LSDA+U energy functional as external parameters and have to be determined independently. We tried several approximations to obtain Hubbard U in this work and decided on the value $U = 4$ eV and $J = 0.97$ eV. These are used throughout the paper.

The value of U can be estimated from the photoemission spectroscopy and x-ray Bremsstrahlung isochromat spectroscopy experiments. Because of difficulties with unambiguous determination of U it can be considered as a parameter of the model. Its value can therefore be adjusted to achieve the best agreement of the results of LSDA+U calculations with photoemission or optical spectra [64]. While the use of an adjustable parameter is generally considered an anathema among first-principles practitioners, the LSDA+U approach does offer a plausible and practical method to approximately treat strongly correlated orbitals in solids. The Hubbard U and exchange parameter J can be determined from supercell LSDA calculations using Slater's transition state technique [65,66] or from constrained LSDA calculations (cLSDA) [66–68]. Recent extensions of the cLSDA method may be found in Refs. [69,70]. The cLSDA method, however, is known from early on to yield values of U that are too large in some cases [71]. For example, Anisimov and Gunnarsson [65] computed the effective on-site Coulomb interaction in metallic Fe and Ce. For Ce the calculated Coulomb interaction was found to be about 6 eV in good agreement with empirical and experimental estimates ranging from 5 to 7 eV. The result for Fe (also about 6 eV) was surprisingly high since U was expected to be in the range of 2–3 eV for elemental transition metals, with the exception of Ni [72,73]. We applied the cLSDA method to MnBi and obtained $U = 4.57$ eV, $J = 0.97$ eV.

Another method for determining the effective interaction is a scheme based on the random-phase approximation (RPA). Early attempts of this can be found in Refs. [74,75]. A method for calculating the Hubbard U, called the constrained RPA (cRPA) scheme was proposed by Aryasetiawan *et al.* [76] some years ago. Subsequently, a combined cLSDA and cRPA method was also proposed [77]. The main merit of the cRPA method over currently available methods is that it allows for a precise elimination of screening channels. They are instead to be included in a more sophisticated treatment of the model Hamiltonian [78]. This method allows easy access to obtaining not only on-site matrix elements but also off-site matrix elements as well as screened-exchange matrix elements. These are usually taken to be the atomic value. Another merit is the possibility of obtaining the frequency-dependent Hubbard U, and may prove to be important. The cRPA method has now been applied to a number of systems with success [71,79–81].

We have calculated an effective interaction for MnBi using a general method of cRPA proposed by Aryasetiawan *et al.* [76]. In this method one divides the full polarizability $P(\mathbf{r},\mathbf{r}';\nu)$ into two parts: the first part $P^d(\mathbf{r},\mathbf{r}';\nu)$ which is defined by all transitions strictly between chosen (usually strongly correlated) eigenstates of one-particle Hamiltonian, and the second part $P^r(\mathbf{r},\mathbf{r}';\nu) = P(\mathbf{r},\mathbf{r}';\nu) - P^d(\mathbf{r},\mathbf{r}';\nu)$. After that, the effective interaction $U(\mathbf{q};\nu)$ can equivalently be found either using $P^d(\mathbf{q};\nu)$ (we write the equations in $\mathbf{q}$ space and

omit product-basis indexes for brevity here),

$$[1 + W(\mathbf{q};\nu)P^d(\mathbf{q};\nu)]U(\mathbf{q};\nu) = W(\mathbf{q};\nu), \qquad (8)$$

or using $P^r(\mathbf{q};\nu)$,

$$[1 - V(\mathbf{q})P^r(\mathbf{q};\nu)]U(\mathbf{q};\nu) = V(\mathbf{q}). \qquad (9)$$

At this point, it is extremely important to understand that such defined partial polarizabilities P^d and P^r both should possess proper asymptotic behavior at small $\mathbf{q}$ (namely, their $P^{\mathbf{q}}_{\mathbf{G}=\mathbf{G}'=0}$ components in plane-wave representation should be proportional to q^2) in order to cancel the corresponding $1/q^2$ divergency in $V(\mathbf{q})$ or $W(\mathbf{q};\nu)$ as seen from the above equations.

It is easy to show that the above requirement is automatically satisfied when one uses band eigenstates of some Hamiltonian of the solid to construct the polarizabilities. But the orbital character of the selected bands does not always correspond perfectly to the character of orbitals in which we are interested.

Therefore in our present work, we follow this procedure: we pick up the bands with proper orbital character (of course we admix some amount of wrong orbital character in this way). Having the proper bands (d bands) picked up for every $\mathbf{k}$ point we calculate d polarizability $P^d(\mathbf{r},\mathbf{r}')$ which comes only from these bands. We perform this in $\mathbf{q}$ space,

$$P^{d,\mathbf{q}}_{ij}(\tau) = - \sum_{\mathbf{k}} \sum_{\lambda\lambda'\lambda''\lambda'''} \sum_{\alpha} \langle M_i^{\mathbf{q}}\Psi_{\lambda'''}^{\alpha\mathbf{k}-\mathbf{q}}|\Psi_\lambda^{\alpha\mathbf{k}}\rangle G_{\lambda\lambda'}^{\alpha\mathbf{k}}(\tau)$$
$$\times \langle \Psi_{\lambda'}^{\alpha\mathbf{k}}|\Psi_{\lambda''}^{\alpha\mathbf{k}-\mathbf{q}}M_j^{\mathbf{q}}\rangle G_{\lambda''\lambda'''}^{\alpha\mathbf{k}-\mathbf{q}}(\beta - \tau), \qquad (10)$$

where α is the spin index, and the summations are performed over the group of d bands only. In (10), $G_{\lambda\lambda'}^{\alpha\mathbf{k}}(\tau)$ is a full GW Green's function which we express in the basis of LDA bands (indexes $\lambda,\lambda',\lambda'',\lambda'''$). The above d polarizability defines an effective interaction among 3d electrons $U_d(\mathbf{r},\mathbf{r}')$ which we again calculate in $\mathbf{q}$ space: $U_d^{-1}(\mathbf{q}) = W^{-1}(\mathbf{q}) + P^d(\mathbf{q})$, and in product basis representation.

Finally, we calculate matrix elements of such found U_d in a basis of atomic orbitals

$$\mathcal{U}_{LL';L''L'''}(\nu) = \sum_{\alpha\alpha'} \int d\mathbf{r} \int d\mathbf{r}'$$
$$\times \varphi_L^*(\mathbf{r})\varphi_{L'}(\mathbf{r})U_{\mathbf{r}\mathbf{r}'}^d(\nu)\varphi_{L'''}^*(\mathbf{r}')\varphi_{L''}(\mathbf{r}'), \quad (11)$$

where the integrations are performed over the corresponding muffin-tin (MT) sphere where 3d orbitals are defined. As atomic orbitals we use the solutions of radial equations inside of the MT spheres (which we define when we solve LDA equations).

Having calculated the full matrix we average it to obtain the effective value U,

$$U(\nu) = \frac{1}{N_d^2} \sum_{LL'} \mathcal{U}_{LL;L'L'}(\nu), \qquad (12)$$

where N_d is the degeneracy of d set.

As follows, our method does not use mapping onto Wannier representation like in the work by Miyake *et al.* [82]. We think, however, for materials with well localized d electrons, the resulting effective interaction is not sensitive to such details. In our opinion, much more important is the question, which
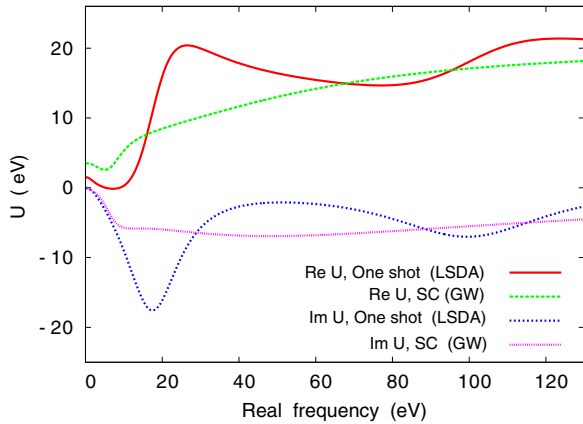
FIG. 2. (Color online) Real and imaginary parts of the partially screened effective interaction U for $3d$ shell of Mn for ferromagnetic MnBi analytically continued to the real axis. One-shot GW (starting with LSDA) and self-consistent GW results.

Green's function (LDA, quasi particle, or self-consistent GW) is used when one calculates full and d polarizabilities.

We have performed one shot (starting with LSDA) and fully self-consistent GW calculations. We have used the mesh of k points $6 \times 6 \times 6$ in Brillouin zone (results obtained with $4 \times 4 \times 4$ k mesh differ very little). Green's function was expanded over the full-potential linearized augmented-plane-wave (FLAPW) band Bloch states [83]. The number of bands in this expansion was 222–240 depending on the **k** point. Inside the MT spheres we have expanded the functions of the fermionic type (Green's function and self-energy) in spherical harmonics up to $L_{\max} = 4$. Bosonic functions (polarizability and interaction) have been expanded up to $L_{\max} = 6$. In the interstitial region, each function was expanded in plane waves. We have used more plane waves for the bosonic functions (340) than for fermionic ones. Our full basis size to expand the bosonic functions (add muffin-tin and interstitial) was about 880 functions depending again on the point in the Brillouin zone. We calculated the effective U as a function of Matsubara frequency and then we analytically continued it to the real frequency axis.

We present in Fig. 2 our calculated effective interaction U for MnBi obtained in one-shot GW and self-consistent GW calculations. The one-shot result for U at zero frequency is about 2 eV whereas the result from self-consistent calculation is approximately 3.6 eV; both of them are smaller than the cLSDA value of 4.57 eV. As mentioned above, the cLSDA method usually overestimates the values of U for transition metals. On the other hand, the cRPA underestimates Hubbard U. Therefore, in our calculations we use $U = 4$ eV and $J = 0.97$ eV, and we use them throughout the paper.

III. ENERGY BAND STRUCTURE

Figure 3 shows the spin-polarized energy band structure of MnBi calculated in the LSDA without SO interaction (two upper panels), fully relativistic Dirac approximation (LSDA+SO, third panel from the top), and a fully relativistic Dirac LSDA+SO+U approximation (lower panel). The
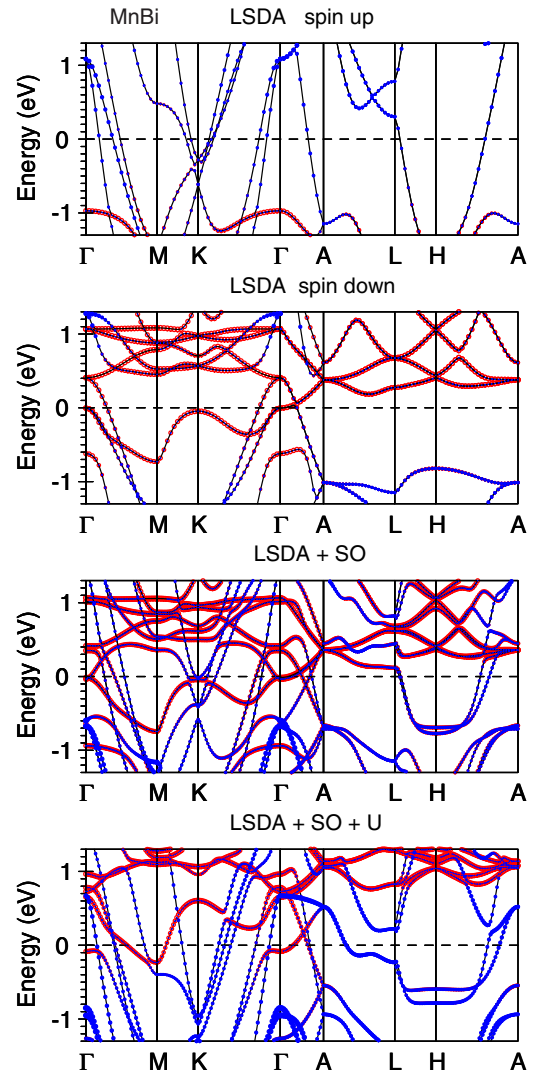

FIG. 3. (Color online) Energy band structure of MnBi in close vicinity of the Fermi level using "fat band" representation: a nonrelativistic (two upper panels), fully relativistic (third panel from the top), and fully relativistic LSDA+SO+U (lower panel) energy bands.

LSDA+SO results are in good agreement with previous LSDA studies [40–44]. In "fat band" representation, the open red circles show the Mn $3d$ character of the wave function in each **k** point. Closed blue circles indicate the Bi $6p$ character. The larger circle corresponds to the larger contribution of the corresponding character in the wave function for a given **k** point.

The splitting of the energy bands in the H and A symmetry point in the -0.6 to -1 eV energy interval is enhanced more than two times after the inclusion of the Coulomb repulsion (compare third panel from the top with lower panel in Fig. 3). Due to the shift of Mn $3d$ states from the Fermi level in the LSDA+SO+U approach the character of the electronic states at the Fermi level are changed towards the decreasing of a Mn $3d$ partial contribution at the Fermi level.

Figure 4 shows partial densities of states for MnBi calculated within LSDA+SO as well as LSDA+SO+U. The Mn d
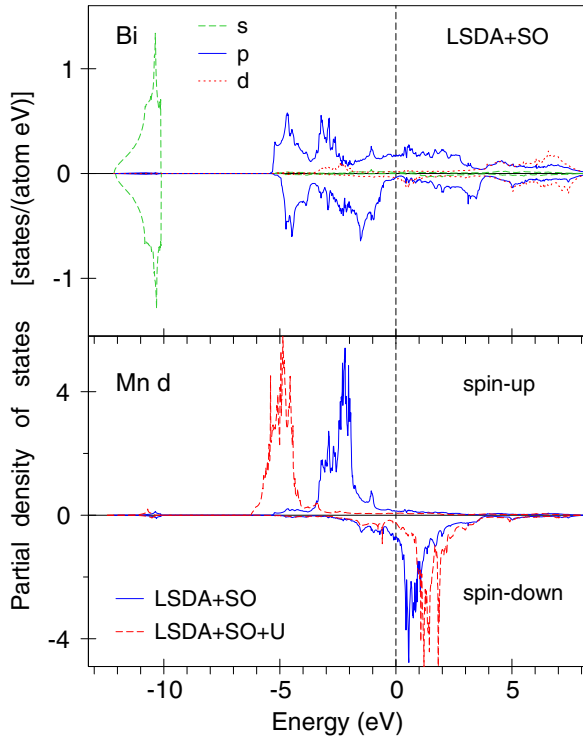
FIG. 4. (Color online) The LSDA+SO and LSDA+SO+U partial densities of states for MnBi.

states are split by the on-site exchange interaction into nearly completely filled majority-spin and unoccupied minority-spin states. The crystal field at the Mn site (D_{3d} point symmetry) causes the splitting of d orbitals into a singlet a_{1g} ($3z^2 - 1$) and two doublets e_g (yz and xz) and e_{g1} (xy and $x^2 - y^2$). Bi $6s$ states situate -12.2 to -10.3 eV below the Fermi level. Bi $6p$ states occupy the -5.2 to 7.5 eV energy range and strongly hybridize with Mn $3d$ states in the -4 to 3 eV energy range. The spin splitting of the Bi p states is quite small. The LSDA+U Mn $3d$ partial DOSs are also presented in Fig. 4. Usually the failure of the LSDA method generally occurs toward the right end of the $3d$ transition-metal series. For Mn, which is in the middle of the $3d$ series, no strong correlation would be expected. As can be seen below, however, the correlation effects are quite important in MnBi for a correct description of the MO properties as well as the MAE.

Our fully relativistic LSDA band structure calculations produce M_s of $3.572\mu_B$ at the Mn site in MnBi. The M_s of $-0.114\mu_B$ induced at the Bi site is antiparallel to that of Mn. The orbital magnetic moment (M_l) at the Mn and Bi sites are equal to $0.156\mu_B$ and $-0.028\mu_B$, respectively. An additional empty sphere also carries small M_s and M_l of $-0.015\mu_B$ and $0.001\mu_B$, respectively. The net magnetic moment in the fully relativistic LSDA band structure calculations is equal to $3.572\mu_B$. Experimental numbers have been obtained for different samples and for samples of different purity in a range from $3.82\mu_B$, [84] to $4.25\mu_B$ [85]. For most pure samples, the moment is close to $4.1\mu_B$ and compares favorably with our LSDA+SO+U moment ($4.172\mu_B$). The spin and orbital magnetic moments in the LSDA+SO+U approach at the

Mn site are equal to $4.224\mu_B$ and $0.125\mu_B$, respectively, and $M_s = -0.134\mu_B$ and $M_l = -0.030\mu_B$ at the Bi site.

The opposite sign of M_s on Mn and Bi atoms can be understood already from Fig. 4. In the LSDA, the DOS of Mn d states near the Fermi level is much larger for a nearly empty spin down electronic band. The latter band just starts to populate in Mn reflecting typical more-than-half-filled d-band behavior. For p states of Bi (upper panel of Fig. 4) the situation is opposite: The population of p states and their induced magnetic moments are relatively small, with a larger DOS for p states for spin up.

The presence of a large amount of Mn spin-down and Bi spin-up electrons at and near the Fermi level creates favorable conditions for the appearance of the large transversal p-d transitions induced by SO coupling.

IV. GROUND STATE PROPERTIES

A. Fermi surface

In this section we present the topology of Fermi surface of MnBi as well as the de Haas–van Alphen (dHvA) extremal cross sections and cyclotron masses.

Figure 5 shows the calculated cross-sectional areas of MnBi FS in the plane perpendicular to the z direction $k_z = 0$ crossed Γ symmetry point using a nonrelativistic method (upper panel), and fully relativistic LSDA+SO (middle panel) and fully relativistic LSDA+SO+U (lower panel) approximations. Figure 6 shows the sheets of the FS in MnBi calculated with the LSDA+SO (left panels) and LSDA+SO+U (right panels) approximations. The inclusion of the SO interaction changes the topology of the FS in MnBi (Fig. 5). Instead of two sheets in the K symmetry point in the LSDA calculations we have only one electron FS. Besides, there are four FS cross sections in the $k_z = 0$ plane in the spin-polarized calculations and three in the LSDA+SO calculations.

There are five sheets of the FS in the LSDA+SO calculations. Almost spherical closed hole FS centered approximately at a half distance between Γ and A symmetry points in Fig. 6(a), has pure Mn $3d$ character. The 23, 24, and 25 hole FSs opened along the Γ-A direction with sixfold symmetry in Figs. 6(c), 6(e), and 6(g), respectively, are mostly due to Bi $6p$ states with small amounts of Mn $3d$ states mixed in. A closed electron FS centered in the K symmetry point in Fig. 6(i) is the mix of Mn $3d$ and Bi $6p$ character.

Inclusion of the Coulomb repulsion increases the size of the 22nd hole FS in Fig. 6(b) and reconstructs the 24th and 25th hole FSs in Figs. 6(f) and 6(h). It produces a new hole FS sheet [see Fig. 6(k)] shown by dashed black curve in the lower panel of Fig. 5 and an additional closed electron FS centered in M symmetry point (lower panel of Fig. 5).

Figure 7 presents the angular variations of the theoretically calculated dHvA frequencies in MnBi in the LSDA+SO+U approximations for field direction in the $(10\bar{1}0)$, $(11\bar{2}0)$, and (0001) planes. The obtained six different types of orbits α, β, γ, δ, ε, and σ belong to the FSs derived by the crossing of the 22nd, 23rd, 24th, 25th, 26th, and 27th energy bands, respectively. The α orbits are situated at the almost spherical closed hole FS which is centered at a half distance between the Γ and A symmetry points [Fig. 6(b)]. Due to smallness and
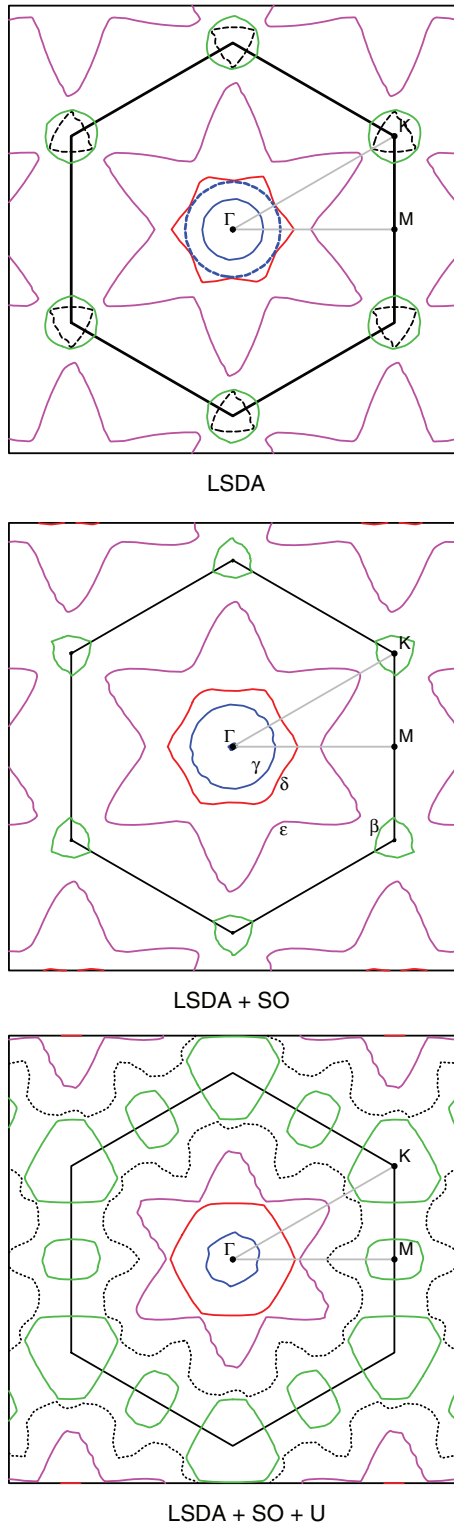
LSDA

LSDA + SO

LSDA + SO + U

FIG. 5. (Color online) The calculated cross sections of MnBi FS in the plane perpendicular to the z direction $k_z = 0$ using a nonrelativistic approach (upper panel), LSDA+SO (middle panel), and LSDA+SO+U ($U = 4$ eV) (lower panel).

(a)   (b)

(c)   (d)

(e)   (f)

(g)   (h)

(i)   (j)

(k)

FIG. 6. The LSDA+SO (left panels) and the LSDA+SO+U (right panels) sheets of MnBi Fermi surface.

the almost spherical shape of these sheets the corresponding dHvA frequencies are rather small and have almost constant angle dependence. The β oscillations belong to electron FS around the K and M points. These orbits split for three separate

β_1, β_2, and β_3 orbits. The β_3 oscillations belong to the closed electron FS sheets around the M symmetry point. The β_1 and β_2 orbits are at the electron FS around the K point (see Fig. 5, lower panel). The γ and δ orbits exist in wide angle intervals at
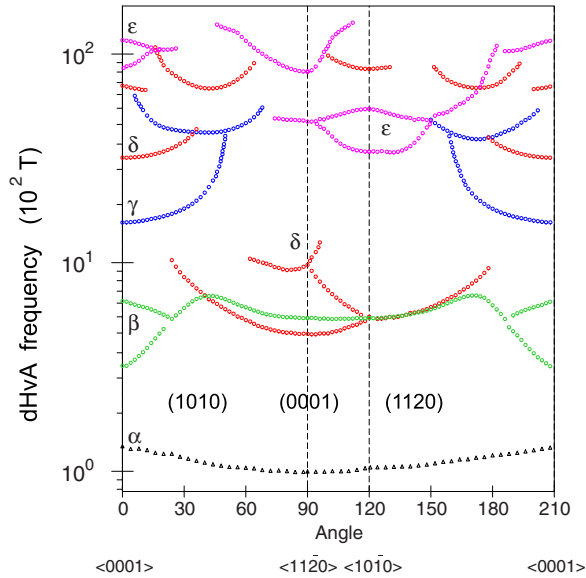
FIG. 7. (Color online) The calculated angular dependence of the dHvA oscillation frequencies in MnBi using LSDA+SO+U (U = 4 eV) approximation.

all three planes. The highest dHvA frequencies were observed for the ε orbits situated at the hole surface derived from the 26th energy band.

We also calculated the angular dependence of the cyclotron masses for MnBi in the LSDA+SO+U approach (not shown). The masses for the low-frequency oscillations α range from $-1.0m_0$ to $-0.65m_0$, and the dHvA β orbits on the electron FS sheet around the K symmetry point possess relatively small cyclotron masses from $0.5m_0$ to $0.8m_0$. The δ orbits also have relatively small cyclotron masses of $-0.8m_0$ to $-0.4m_0$. However, some branches of the δ orbits possess cyclotron masses more than $2m_0$. The masses for the high-frequency oscillations ε are large.

To show how sensitive are the calculations of the FS to the value of Hubbard U, we run additional LSDA+SO+SO calculations with Hubbard U = 3.5 and 4.5 eV. Figure 8 shows the calculated cross sections of MnBi FS for U = 3.5 eV and U = 4.5 eV. After comparing this figure with Fig. 5 for U = 4.0 eV, we can conclude qualitatively that all three calculations produce similar FSs with small changes in the size and the shape of some FS sheets.

However, the dHvA oscillations are quite sensitive to the value of Hubbard U. The frequencies of the α orbits are significantly reduced for U = 3.5 eV and increased for U = 4.5 eV in comparison with U = 4.0 eV calculations. The δ and ε orbits have an opposite U behavior: their frequencies are decreased with the increase of U. On the other hand, the σ and γ orbits are less sensitive to the value of U.

The experimental measurement of the dHvA effect is highly desired, as it will answer which value of Hubbard U is realized in MnBi (Fig. 9). From the experimental point of view it would be no problem to measure the dHvA oscillations in MnBi due to relatively small cyclotron masses for most dHvA orbits. However, a single crystal sample of good quality might be needed.
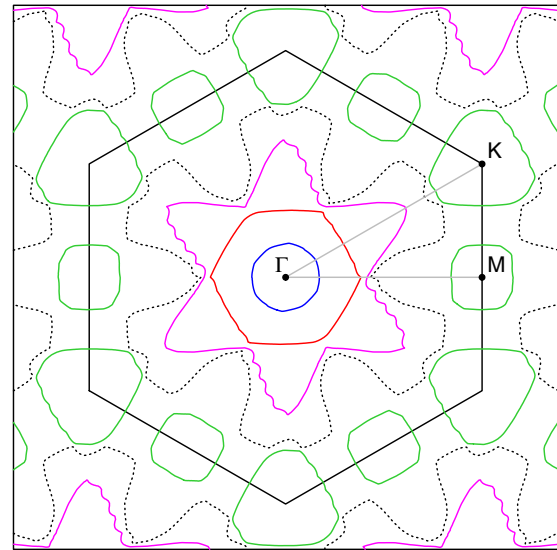
LSDA + SO + U   U=3.5 eV
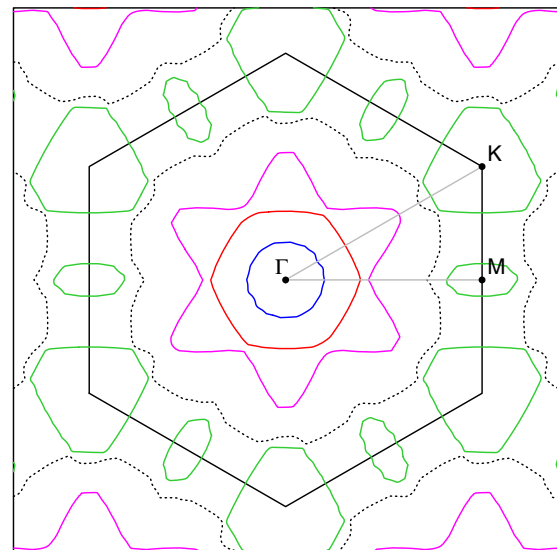
LSDA + SO + U   U=4.5 eV

FIG. 8. (Color online) The calculated cross sections of MnBi FS in the plane perpendicular to the z direction $k_z = 0$ using the fully relativistic LSDA+SO+U method for U = 3.5 eV (upper panel) and U = 4.5 eV (lower panel).

B. Magnetocrystalline anisotropy

It has been established that such unique temperature dependence of the coercivity and MAE in MnBi is determined by the thermal variation of the lattice parameters a and c. In the following section we explain experimental observations by examining the dependence of calculated total energy and MAE on the lattice geometry. We assume that the finite temperature can be mimicked by the lattice constants corresponding to this temperature. We confirm that spin reorientation arises from a change of sign in MAE, which depends on the lattice constants.

Figure 10 shows the experimentally measured temperature dependence of the lattice constants a and c according to Refs. [85,86] together with the magnetization [85] in MnBi.
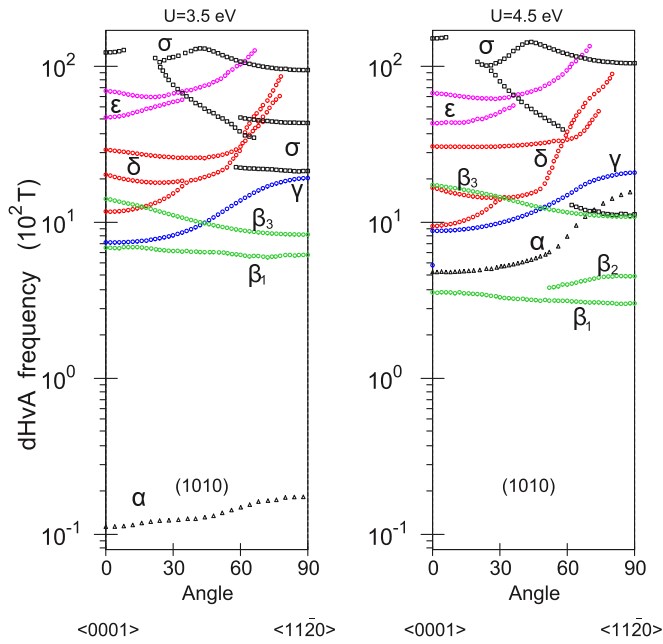
FIG. 9. (Color online) The calculated angular dependence of the dHvA oscillation frequencies in MnBi using LSDA+SO+U approximation for $U = 3.5$ eV (left panel) and $U = 4.5$ eV (right panel).

FIG. 10. (Color online) The temperature dependence of the lattice parameters a and c (upper and middle panels, respectively) of MnBi according to Refs. [85] (blue curve) and [86] (red curve). The lower panel shows temperature dependence of magnetization in MnBi [85].

Yang *et al.* [85] measured temperature dependence of the lattice parameters a and c in a wide temperature range from 10 to 700 K. Koyoma *et al.* [86], on the other hand, used a smaller temperature interval (10–300 K). They did use a very fine temperature mesh in the vicinity of T_{SR}. Both measurements show similar behavior for the lattice constant a, but strongly differ from each other in the temperature behavior of lattice constant c. The results of Yang *et al.* [85] show a rather smooth decrease of parameter c with decreasing of T below T_{SR}. Koyama *et al.* [86] found a discontinuous behavior of constant c near T_{SR} (Fig. 10).

Figure 11 shows the MAE as a function of the polar angle θ and temperature calculated with the LSDA+SO and the LSDA+SO+U methods. Here we used the temperature dependence of the lattice constants a and c obtained by Yang *et al.* [85]. The LSDA+SO approach gives the value of MAE equal to -2.2 meV/cell at zero temperature. This value is in good agreement with a previous FLAPW band structure calculation by Ravindran *et al.* [35] (-2.0 meV/cell). However, both of these values are an order of magnitude larger than the experimental value of -0.13 meV/cell [18,87]. Besides, the LSDA+SO approximation shows that the easy direction of the magnetization is in the basal plane for any value of lattice constant a and axial ratio c/a (meaning the entire temperature range), and therefore provides no explanation of the spin-reorientation observed experimentally at the $T_{SR} \sim 90$ K. On the other hand, the LSDA+SO+U approach gives the value of MAE equal to -0.39 meV/cell at zero temperature. This value is already in better agreement with the experiment, but still nearly three times larger than the experimentally estimated value of -0.13 meV/cell [18,87]. Thus the inclusion of the Coulomb correlations provides a correct easy magnetization
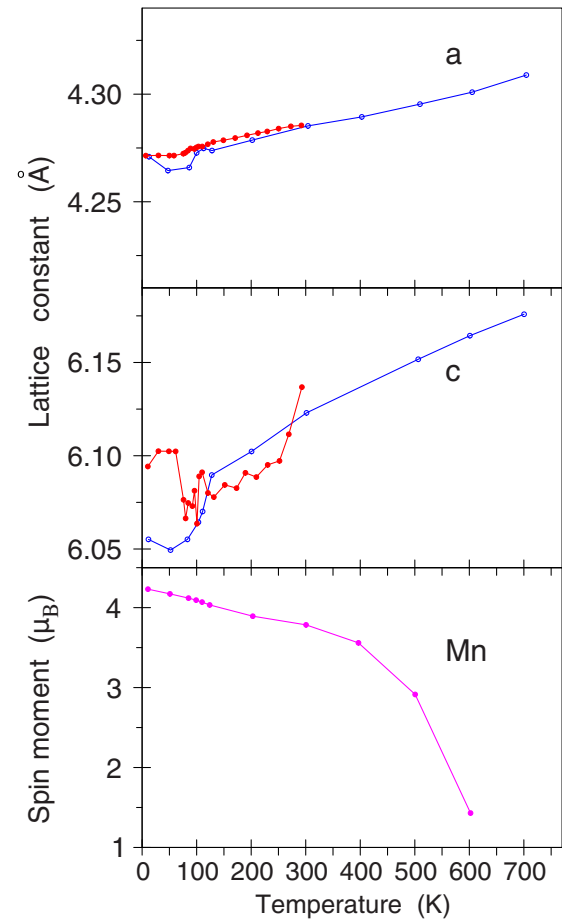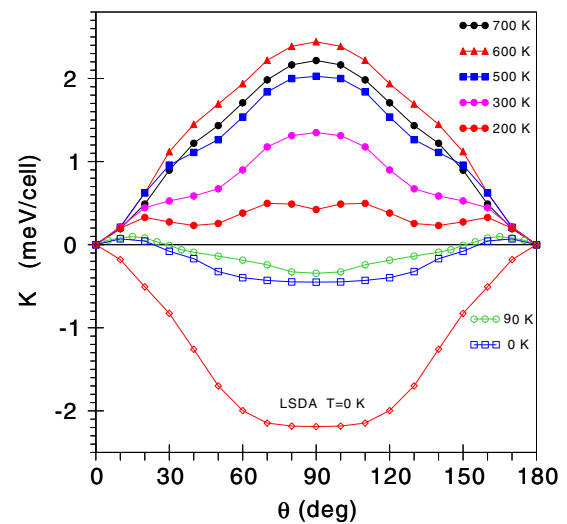

FIG. 11. (Color online) The MAE K as a function of the polar angle θ and temperature in MnBi calculated in the LSDA+SO (open blue squares) and the LSDA+SO+U methods. The temperature dependence of the lattice constants a and c is from Ref. [85].
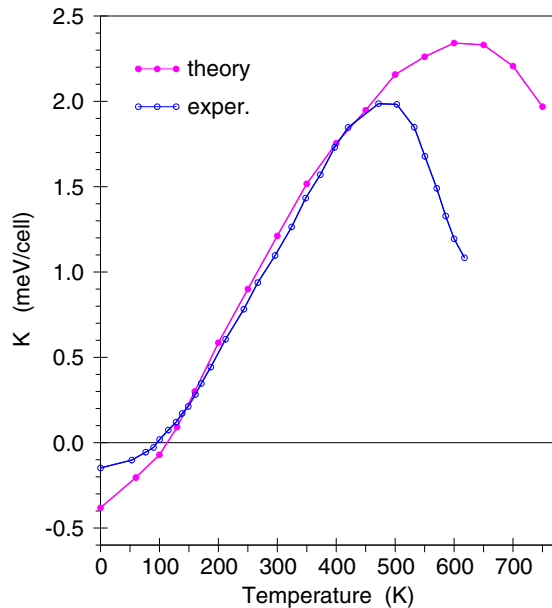
FIG. 12. (Color online) Theoretically calculated temperature dependence of the MAE K in MnBi using the LSDA+SO+U in comparison with the experiment [18].

FIG. 13. (Color online) The LSDA+SO+U calculations of the MAE K as a function of the polar angle θ for the lattice constant $c = 6.123$ Å. This corresponds to the $T = 300$ K and $a = 4.272$ Å (curve 1) and $a = 4.283$ Å (curve 2) corresponding to $T = 100$ and 300 K, respectively [85].

direction along the c axis for the temperatures above T_{SR1} and in the plane below T_{SR} for the experimental parameters a and c.

Figure 12 presents the theoretically calculated temperature dependence of the MAE in MnBi using the LSDA+SO+U approximation in comparison with the experiment [18]. The theoretical MAE is in very good agreement with the experiment in the 150 to 450 K temperature range. Thus, our calculations confirm the experimental claim [86] that the unusual temperature dependence of MAE is primarily due to a specific lattice thermal expansion.

To determine a major source of MAE we expanded MAE over SO coupling parameters by directly varying these parameters on different sites and fitting the resulting MAE with on-site and intersite contribution functions. This analysis has shown that the dominant contribution to the MAE variation is produced by the anisotropic pairwise interaction between p states of Bi atoms. Thus, the spin reorientation observed in MnBi at 90 K can be considered as Bi-Bi anisotropic pair exchange striction driven transition. Further studies of this inversion of the anisotropic exchange in materials with spin reorientation are needed. On this stage, we can conclude that the major contribution to the MAE in MnBi is produced by weakly polarized Bi subsystem with dominant interatomic anisotropic Neel's type interactions.

With the temperature increase above RT, the experimentally measured anisotropy energy increases and reaches its maximum at around 500 K, and then rapidly decreases at higher temperatures. The LSDA+SO+U results show the same temperature behavior. They, however, show higher MAE in the maximum. Besides, the theoretically calculated maximum of the MAE shifts towards higher temperatures (Fig. 12). Such disagreement between theory and experiment might be due to the magnetic spin disorder effect. The temperature dependence of magnetization in MnBi measured by Yang *et al.* [85] shows
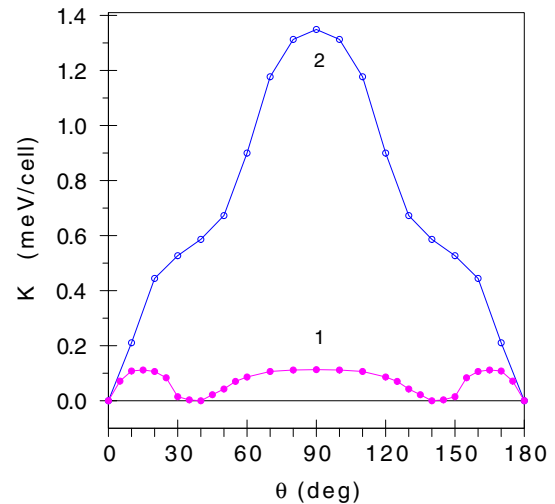
a drastic reduction of the magnetization from $4.25\mu_B$ at 0 K to $1.43\mu_B$ for 600 K. This presumably is due to spin disorder (see the lower panel of Fig. 10). Such an effect has not been taken into account in our calculations.

We found a strong dependence of the MAE on in-plane lattice constant a. Figure 13 shows the MAE as a function of the polar angle θ for the lattice constant $c = 6.123$ Å. This corresponds to $T = 300$ K, and $a = 4.272$ Å (curve 1) and $a = 4.283$ Å (curve 2) corresponding to $T = 100$ and 300 K, respectively [85]. Expansion of in-plane lattice constant a by 0.01 Å occurs from 100 K, and 300 K increases the MAE by approximately 1.2 meV. Corresponding results for c parameter expansion produce a much smaller result of 0.1 meV (Fig. 13).

To investigate the MAE as a function of the polar angle θ in the vicinity of the spin reorientation phase transition, we fixed the lattice constant a for the spin-reorientation temperature $a = 4.274$ Å [86] and vary c from $c = 6.09$ Å to $c = 6.14$ Å with a step of 0.01 Å (Fig. 14). For the lattice constants $c = 6.09$ Å, $c = 6.10$ Å, and $c = 6.11$ Å (curves 1–3, respectively), the easy magnetization direction is in the basal plane. There are two local minima in the total energy for the $c = 6.12$ Å (curve 4): one along the c direction and at $\theta \sim 41°$ with a barrier in between. The last angle is close to the experimentally measured $\theta_{\text{exper}} = 37°$ at $T_{SR} = 90$ K where the magnetization flops into the ab basal plane [17] (see Fig. 15). For larger values of the lattice constant c, the easy magnetization direction is along the c direction in agreement with experimental observation. We would like to point out that the results presented in Fig. 14 have to be considered only as qualitative ones because by fixing the constant a and varying c, the c/a has altered the overall volume per unit cell.

The results shown in Fig. 14 lead to some interesting conclusions. The angular dependence of the total energy demonstrates the presence of a "double-well" potential. This fact leads to a hysteresis phenomenon as a function of temperature. For instance, one can expect a nonsmooth dependence of the
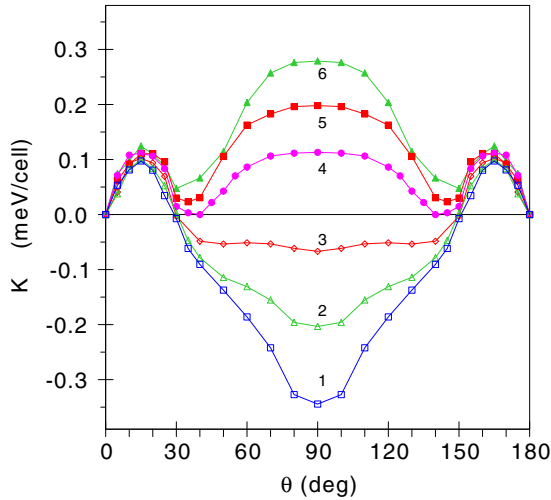
FIG. 14. (Color online) The LSDA+SO+U calculations of the MAE K as a function of the polar angle θ for the lattice constant $a = 4.274$ Å. This corresponds to the spin reorientation ($T_{SR} = 90$ K) [86] and $c = 6.09$ Å (curve 1), $c = 6.10$ Å (curve 2), $c = 6.11$ Å (curve 3), $c = 6.12$ Å (curve 4), $c = 6.13$ Å (curve 5), and $c = 6.14$ Å (curve 6).

magnetization direction change with a "sudden" switch of easy direction at different temperatures depending on whether a cooling or heating process is being used. This qualitatively explains the nonanalytical dependence of easy axes observed in Ref. [17] (see Fig. 15). The total energy shows a highly nontrivial angular dependence with several minima confirming theoretically a 'jump' of magnetization direction from 90 to approximately 40 degrees observed experimentally at 90 K (Fig. 15). It also leads to a hysteresis behavior of magnetization as a function of temperature. This in turn creates a condition for a noncontinuous spin reorientation transition, that can be considered as a planar to the uniaxial anisotropy phase transition.

One can conclude that the increase of MAE with temperature presented in Fig. 12 is mostly due to changing the in-plane lattice constant a.

We examine the dependence of the MAE on the exchange splitting and the SO interaction. The exchange splitting and the SO coupling are studied by scaling the corresponding terms in the Hamiltonian artificially with a constant prefactor. This
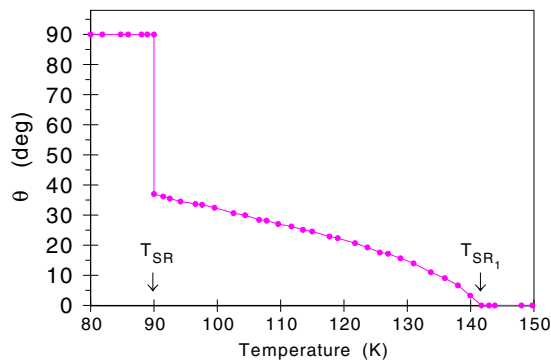

FIG. 15. (Color online) Temperature variation of the polar angle θ between the easy axis of the magnetization and the c axis [17] in MnBi.
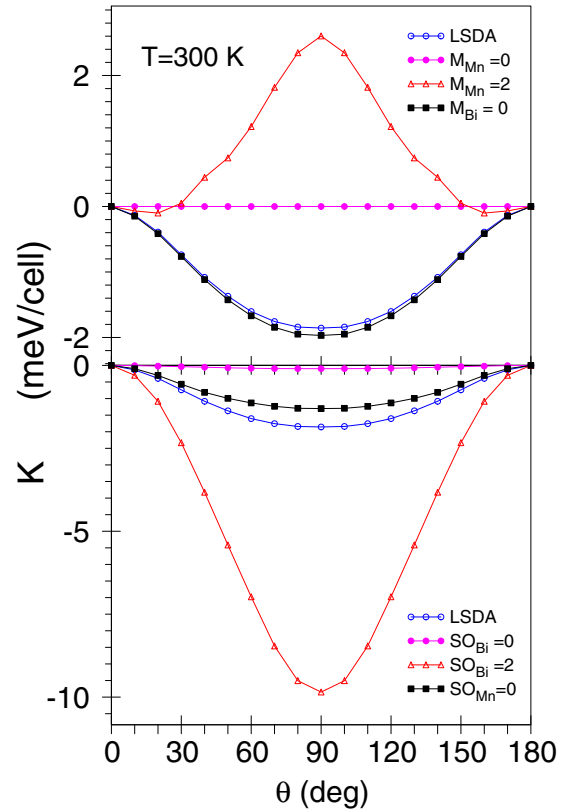

FIG. 16. (Color online) The effect of scaling of the exchange splitting (upper panel) and value of SO constant (lower panel) on either Mn or Bi atoms on the MAE K in MnBi (see the text).

scaling can be atom dependent, i.e., within each atomic sphere. The outcomes of such constraining calculations for the MAE in MnBi are shown in Fig. 16. In the upper panel, the importance of the exchange splitting is illustrated. When the exchange splitting on Bi is set to zero, the MAE is barely modified. But when we performed such operation on Mn atoms, the MAE totally vanishes. Furthermore, an enhancement of the exchange splitting on Mn by a factor of 2.0 (red open triangles) leads to a correct easy magnetization along the z direction. So, two independent methods (LSDA+U and constraining field application) obtained a much better MAE description while increasing magnetic moment on Mn site (strongly underestimated in LSDA). We conclude that the proper value of Mn atom spin moment is most likely crucial for the magnetic anisotropy studies.

The lower panel of Fig. 16 shows the dependence on the SO coupling. If we set SO coupling on Mn to zero, the MAE does not change significantly (full black squares). On the other hand, when the SO coupling on Bi is zero, the MAE almost disappears (magenta full circles). The scaling of the SO coupling of Bi by a factor of 2.0 leads to an increase of the MAE by a factor of 5 confirming a dominant contribution of the SO interaction at the Bi site to the large value of MAE in this compound.

It is customary to relate the MAE with the anisotropy of M_l [orbital moment anisotropy (OMA)] [88–93]. Figure 17 presents the MAE, M_l, OMA, and spin moment anisotropy (SMA) for $T = 0$ K and $T = 300$ K. The M_l, OMA, and SMA are larger at the Mn site than at the Bi one. The OMA is just

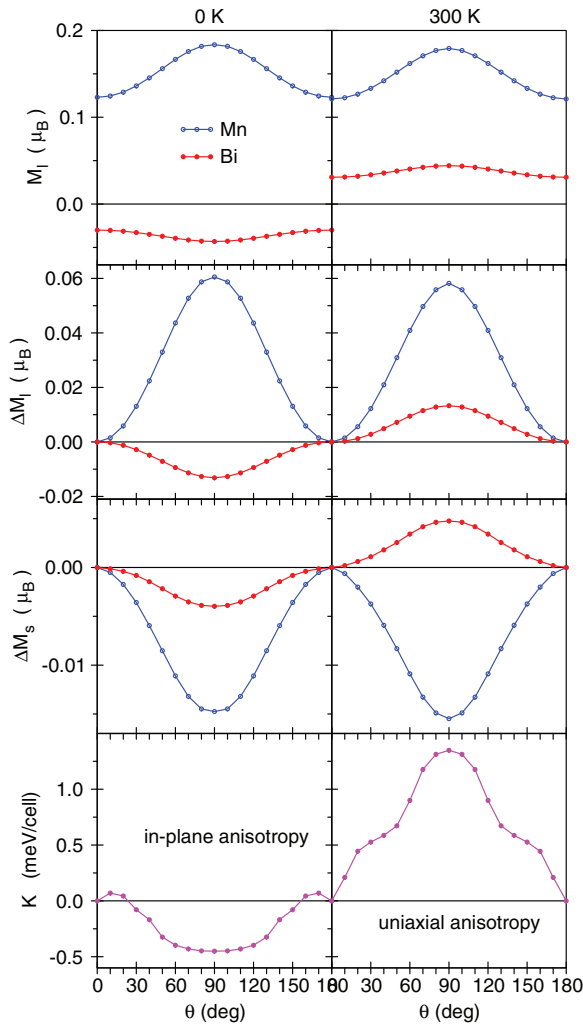FIG. 17. (Color online) The MAE, M_l, OMA (ΔM_l) and SMA (ΔM_s) for $T = 0$ K (left panel) and $T = 300$ K (right panel).

energy, so $K \sim -\frac{1}{4}\lambda\Delta M_l$, which formally corresponds to a Hund's rule for a less than half-filled band. This is similar to the situation in CoPt and FePt, discussed in Ref. [92], where analogous effect has been obtained for nearly filled $5d$ Pt band.

Recently, Zarkevich *et al.* [95] calculated the total energy and MAE versus crystal geometry using perturbative SO interaction inclusion with a Hubbard U correction. They found that this correction improves a comparison of theoretical and experimental MAE and showed that MAE is strongly affected by a. However, their absolute values of MAE are much smaller than the experimental ones. Also, the spin reorientation transition in their calculations occurs at the lattice constants corresponding to approximately 500 K. The differences are probably related to the different treatment of the relativistic effects (for Bi-based systems it can be important), different values of Hubbard parameters, and different LSDA+U schemes.

V. EXCITED STATE PROPERTIES

A. Magneto-optical properties

In this section we provide a theoretical explanation of the MO properties of MnBi.

The experimental Kerr spectra as well as the calculated ones are shown in Fig. 18. The Kerr rotation is denoted by θ_K and the Kerr ellipticity by ε_K. First-principles LSDA theory predicts a very large Kerr rotation in MnBi of about $-2°$ at 1.8 eV. This is even larger than the measured peak value of $-1.6°$ [25]. The experiment shows a second maximum in the Kerr angle at 3.4 eV. Here the LSDA calculations give only a shoulder. We found that the reason for such disagreement is the underestimation of the M_s in the LSDA. The M_s at the Mn site is equal to $3.572\mu_B$ in the LSDA. However, the experimental value at low temperature is equal to $4.25\mu_B$ [85]. In Fig. 18, we present the calculated Kerr spectra in the LSDA+SO+U (red full lines) and the LSDA+SO calculations with an artificially increased exchange splitting on the Mn site by 1.5 times (black dotted curves). In both latter calculations the M_s is quite close to the experimental value ($4.234\mu_B$ and $4.257\mu_B$ for the LSDA+SO+U and the LSDA+SO with increased spin splitting, respectively). Both spectra have similar shapes with much better reproduction of the second maximum in the Kerr angle at 3.4 eV. Another feature of the experimental Kerr rotation is that it exhibits a sign reversal at 0.9 eV. This sign reversal is actually also given by the LSDA+SO method, but for a smaller energy. The LSDA+SO+U method and the LSDA+SO one with increased spin splitting perfectly reproduces the energy of a sign reversal at 0.9 eV. The LSDA+SO+U approximation also better reproduces the observed shape of the Kerr ellipticity and a sign reversal at around 2 eV (see the upper panel of Fig. 18).

The Kerr spectra depend on the MO conductivity spectra in an entangled way. Therefore, it is difficult to assign features in the Kerr spectra to particular band transitions. The absorptive parts of the optical conductivity σ_{1sxx} and σ_{2sxy}, however, relate directly to the interband optical transitions, and therefore provide more physical insight [50,96]. The calculated absorptive part of off-diagonal optical conductivity σ_{2xy} for MnBi is shown in Fig. 19. The main peak in the Kerr rotation
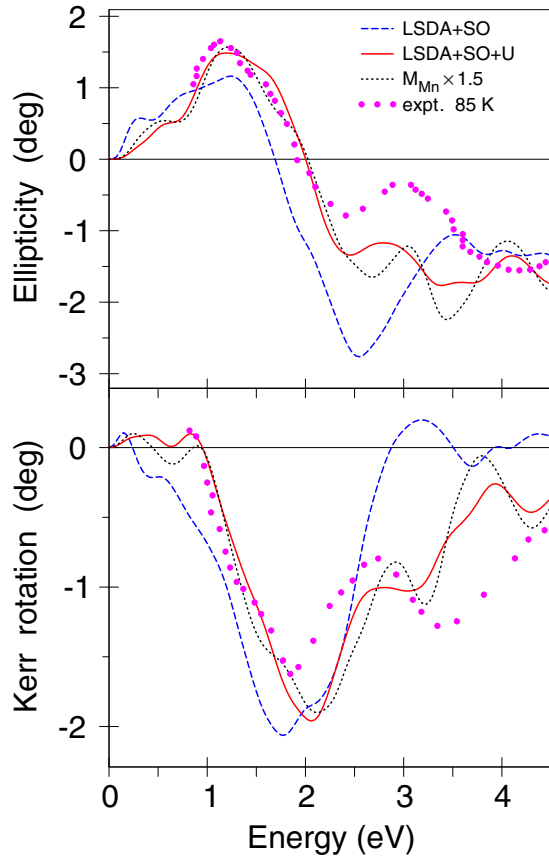
four times larger than the SMA for both sites. It is somewhat unusual as a contribution of spin moment to the anisotropy is normally considered to be negligible. The Bi M_l changes its sign through spin-reorientation transition, therefore the inversion of the MAE in our calculations is directly correlated with the sign inversion of M_l at the Bi site or inversion of antiferromagnetic coupling between spin moment on Mn and orbital moment on Bi atoms.

The MAE is approximately proportional to the OMA through expression $K \sim \frac{1}{4}\lambda\Delta M_l$ [88–93], where λ is the SO parameter (~ 0.041 eV for Mn and ~ 0.85 eV for Bi [94]). Therefore, the major contribution to the MAE is due to the OMA at the Bi site with some contribution from the SMA. A direct proportionality of K and OMA above is directly related to a Hund's rule for the more than half-filled band. However, we argued in Ref. [92] that a difference of DOS at E_f for the different spin channels is more important for the sign of this proportionality. As we discussed above, there are more spin up p states of Bi atom at E_f despite p^3 configuration. This in turn leads to inverse proportionality between K and OMA. Thus, a minimum of orbital moment on Bi site (with more than half filled p band) corresponds to a minimum of the total

FIG. 18. (Color online) Calculated in the LSDA+SO (blue dashed lines) and LSDA+SO+U (red full lines) approximations polar Kerr rotation (θ_K) and Kerr ellipticity (ε_K) spectra of MnBi in comparison with the experimental measurements from Ref. [25]. $M_{Mn} \times 1.5$ denotes an exchange splitting of 150% of the first-principles value.

of MnBi is due to the maximum in σ_{2xy} at 1.8 eV. The second fine structure in the MnBi Kerr spectrum at 3.4 eV corresponds to the high energy peak in σ_{2xy} at the same energy. The LSDA+SO calculations strongly underestimate
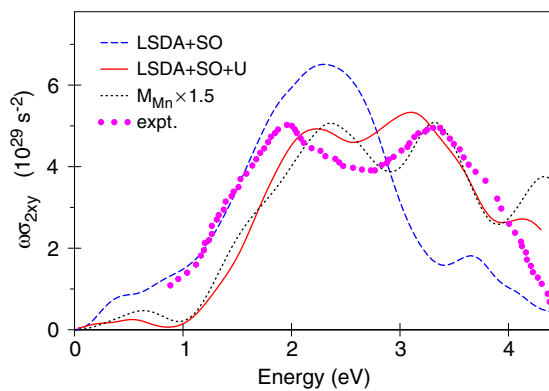

FIG. 19. (Color online) Calculated in the LSDA+SO (blue dashed lines) and LSDA+SO+U (red full lines) approximations off-diagonal component (σ_{2xy}) of the conductivity tensor for MnBi in comparison with the experimental measurements in MnBi from Ref. [25]. $M_{Mn} \times 1.5$ denotes an exchange splitting of 150% of the first-principles value.
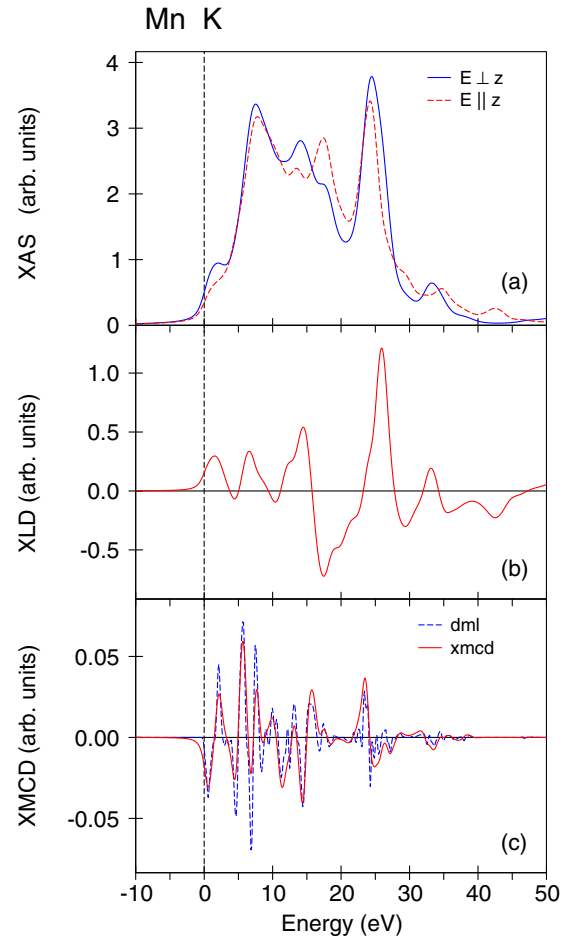

FIG. 20. (Color online) The effect of scaling of the exchange splitting (upper panel) and the value of the SO constant (lower panel) on either Mn or Bi atoms on the MO Kerr spectra in MnBi (see the text).

the intensity of the second high energy peak in σ_{2xy}. As a result of this, the LSDA+SO fails to correctly describe the second negative peak in the Kerr rotation at 3.4 eV. On the other hand, the LSDA+SO+U and the LSDA+SO with increased spin splitting quite well reproduce the intensity of the second high energy peak in the σ_{2xy} spectrum and therefore better describes the 3.4 eV peak in the Kerr rotation.

We can conclude that the main reason for a failure of LDSA to describe the MO properties in MnBi is the significant underestimation of spin magnetic moment on the Mn atom. Two very different techniques (the LSDA+U method and the application of an external magnetic field on the Mn atom) produced similar spin moment enhancement and consequently better MO values.

It is important to identify the origin of the large Kerr effect in MnBi. To this end, we examine the dependence of the MO spectra on the exchange splitting and the SO interaction. The exchange splitting and the SO coupling are studied by scaling the corresponding terms in the Hamiltonian artificially with a constant prefactor. These modifications can be done within each atomic sphere independently, so that we can investigate the separate effects of these quantities on Mn and on Bi. The outcomes of these model calculations for the Kerr rotation of MnBi are shown in Fig. 20. In the lower panel, the importance

of the exchange splitting is illustrated. When the exchange splitting on Bi is set to zero, the Kerr rotation remains as it is. But when we do the same for the exchange splitting on Mn, the Kerr rotation totally vanishes. This implies that the exchange splitting due to Mn is crucial for the sizable Kerr rotation, but that of Bi is not important. Furthermore, an enhancement of the exchange splitting on Mn by a factor of 1.5 (dotted line) leads to a much larger peak in the Kerr rotation at 3.4 eV. The upper panel of Fig. 20 shows the dependence on the SO coupling. If we set the SO coupling on Mn to zero, the Kerr rotation does not change very much (dashed red line). On the other hand, when the SO coupling on Bi is zero, the Kerr rotation almost disappears (dotted magenta line). Thus, the SO coupling of Bi is equally responsible for the large Kerr rotation as is the exchange splitting of Mn. An intermediate scaling of the SO coupling of Bi by a factor of 0.5 leads to an approximately half as large Kerr angle, thereby illustrating the almost linear dependence of the Kerr effect on the SO interaction of Bi in this compound.

B. X-ray magnetic circular dichroism

Motivated by the developing interest in obtaining element specific magnetic moment information provided by XMCD measurements. We calculate the x-ray absorption spectroscopy (XAS) and XMCD spectra of MnBi at the Mn K and L_3, and at the Bi $M_{2,3}$, $M_{4,5}$, $N_{2,3}$, $N_{4,5}$, $N_{6,7}$, and $O_{2,3}$ edges.

Figure 21(a) shows the theoretically calculated x-ray absorption spectra at the Mn K edge in MnBi with the electric field vector of the x rays both parallel (dashed red curve) and perpendicular (full blue curve) to the c axis. The associated x-ray linear dichroism (XLD) signal (obtained by taking the difference of the x-ray absorption spectra for the two polarizations) is given in panel (b) of Fig. 21. Figure 21(c) shows the theoretically calculated XMCD in terms of the difference in absorption $\Delta\mu_K = \mu_K^+ - \mu_K^-$ for left and right circularly polarized radiation in MnBi. After comparing panels (b) and (c), we can conclude that the XMCD signal is almost one order of magnitude smaller than the corresponding XLD signal. Also, the spectra have major peaks in different energy intervals. Major peaks in the XMCD spectrum are mostly located in the 0 to 15 eV energy interval. However, the XML spectrum possesses the major peaks above 15 eV.

Because dipole-allowed transitions dominate the absorption spectrum for unpolarized radiation, the absorption coefficient $\mu_K^0(E)$ reflects primarily the density of states (DOS) of unoccupied $4p$-like states $N_p(E)$ of Mn above the Fermi level. Due to the energy-dependent radial matrix element for the $1s \rightarrow 4p$ transition, there is no strict one-to-one correspondence between $\mu_K(E)$ and $N_p(E)$. The exchange splitting of the initial $1s$-core state is extremely small and therefore only the exchange and SO splitting of the final $4p$ states is responsible for the observed dichroism at the K edge. For this reason, the dichroism is found to be quite small (lower panel of Fig. 21).

To illustrate the influence of SO interaction on the final states involved in the transitions, let us introduce a site-
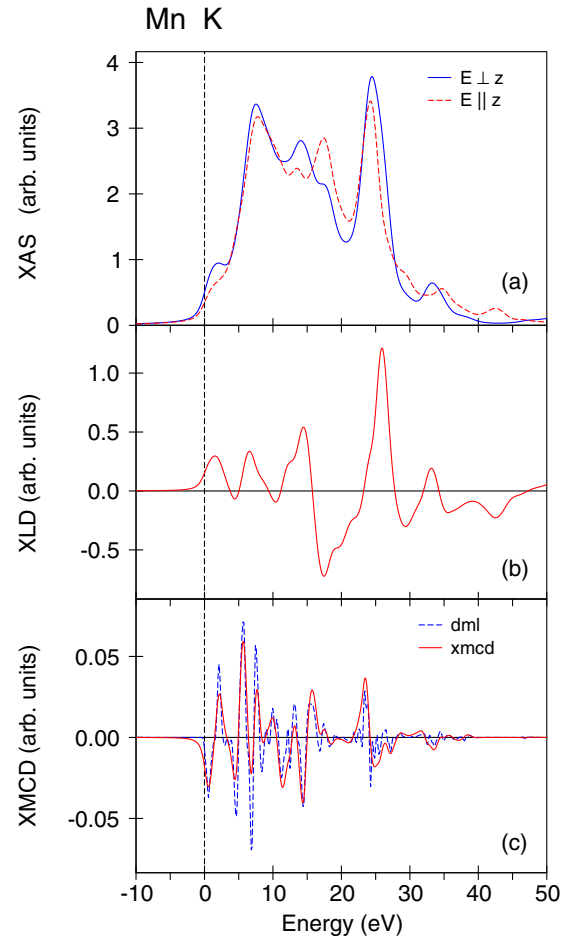

FIG. 21. (Color online) (a) The theoretically calculated x-ray absorption spectra of MnBi at the Mn K edge with the electric field vector of the x rays parallel (red dashed curve) and perpendicular (blue full curve) to the z axis; (b) theoretically calculated XLD spectra at the Mn K edge; (c) the theoretically calculated XMCD spectrum at the Mn K edge (red full curve) and dm_l function (blue dashed curve). The calculations have been done using the LSDA+SO+U approach.

dependent function $dm_{tl}(E)$ given by [97]

$$dm_{tl}(E) = \sum_{m_j} \sum_{n\mathbf{k}} \langle \Psi_{tl}^{n\mathbf{k}} | \hat{l}_z | \Psi_{jm_j} \rangle \delta(E - E_{n\mathbf{k}}), \quad (13)$$

where $\hat{l}_z$ is the z projection of the angular momentum operator, $E_{n\mathbf{k}}$ and $\Psi_{tl}^{n\mathbf{k}}$ are the energy of the nth band and the part of the corresponding LMTO wave function formed by the states with the angular momentum l inside the atomic sphere centered at site t, respectively. In analogy to the l-projected density of states, $dm_{tl}(E)$ can be referred to as the site- and l-projected density of the expectation value of $\hat{l}_z$.

The $4p$-$3d$ hybridization and the SO interaction in the $4p$ states play a crucial role for the Mn K-edge dichroism. As seen in Fig. 21(c), the K XMCD spectrum and $dm_{tl}(E)$ functions are closely related to one another and give a rather simple and straightforward interpretation of the XMCD spectra at the K edge.

Because of the dipole selection rules and apart from the $4s_{1/2}$ states (which have a small contribution to the XAS due to relatively small $2p \rightarrow 4s$ matrix elements [50]), only
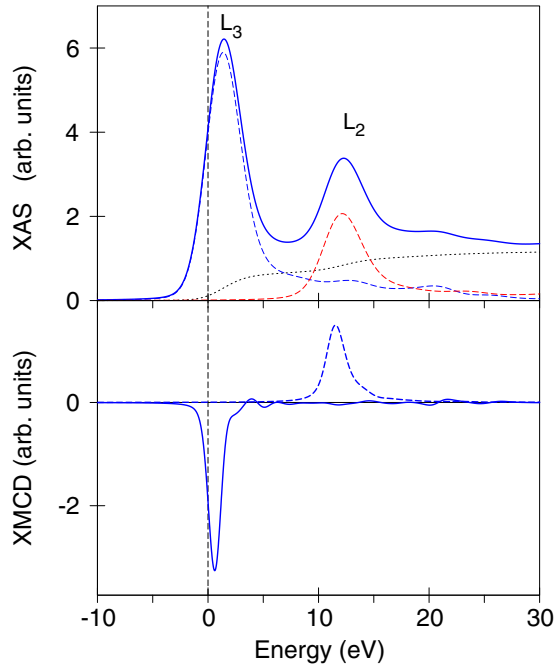
FIG. 22. (Color online) X-ray absorption (top panel) and XMCD spectra (lower panel) at the Mn $L_{2,3}$ edges calculated using the LSDA+SO+U.

$3d_{3/2}$ states occur as final states for L_2 XAS for unpolarized radiation. Whereas for L_3 XAS the $3d_{5/2}$ states also contribute. Although the $2p_{3/2} \rightarrow 3d_{3/2}$ radial matrix elements are only slightly smaller than elements for the $2p_{3/2} \rightarrow 3d_{5/2}$ transitions the angular matrix elements strongly suppress the $2p_{3/2} \rightarrow 3d_{3/2}$ contribution. Therefore in neglecting the energy dependence of the radial matrix elements, the L_2 and the L_3 spectrum can be viewed as a direct mapping of the DOS curve for $3d_{3/2}$ and $3d_{5/2}$ character, respectively.

In contrast to the K edge, the dichroism at the L_2 and L_3 edges is also influenced by the SO coupling of the initial $2p$-core states. This gives rise to a very pronounced dichroism in comparison with the dichroism at the K edge. Figure 22 shows the theoretically calculated Mn $L_{2,3}$ XMCD spectra in MnBi. The XMCD spectra at the $L_{2,3}$ edges are mostly determined by the strength of the SO coupling of the initial $2p$-core states and spin polarization of the final empty $3d_{3/2,5/2}$ states. The exchange splitting of the $2p$-core states as well as the SO coupling of the $3d$-valence states are of minor importance for the XMCD at the $L_{2,3}$ edge of $3d$ transition metals [50].

As mentioned above, XMCD investigations supply information on magnetic properties in a component resolved way. This seems especially interesting if there is a magnetic moment induced at a normally nonmagnetic element by neighboring magnetic atoms. The underlying mechanism of the magnetic and MO properties of the systems considered here is the well known ability of transition metals to induce large spin polarization of Bi via strong $3d$-$6p$ hybridization and exchange interaction.

Results of the theoretical calculations for the circular dichroism at the $L_{2,3}$ edge of Bi are shown in Fig. 23. The XMCD spectrum is negative at the L_3 edge and positive at the L_2 edge as has been seen for the XMCD spectra at the
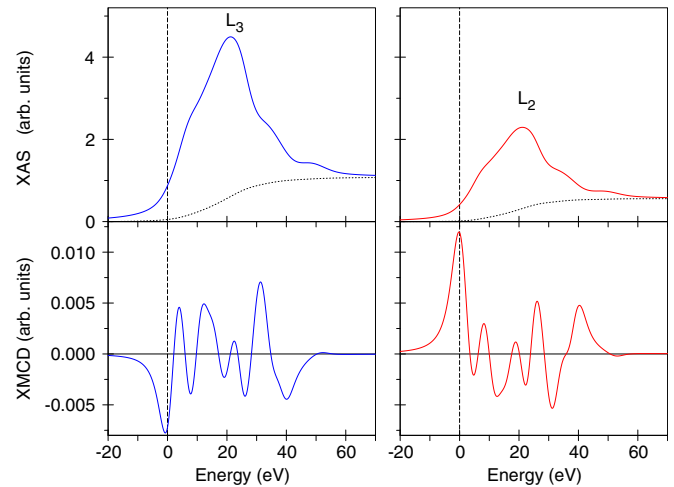

FIG. 23. (Color online) X-ray absorption (top panel) and XMCD spectra (lower panel) at the Bi $L_{2,3}$ edges calculated using the LSDA+SO+U.

$L_{2,3}$ edges of Mn (Fig. 22). The XMCD in Bi at the L_3 and L_2 edges are of nearly equal magnitude. This suggests that an orbital magnetic moment almost vanishes in Bi $5d$ states in MnBi.

To investigate the influence of the initial state on the resulting Bi XMCD spectra, we also calculated the XAS and XMCD spectra of MnBi at the $M_{2,3}$, $M_{4,5}$, $N_{2,3}$, $N_{4,5}$, $N_{6,7}$, and $O_{2,3}$ edges. We found a systematic decreasing of the XMCD spectra in terms of $R = \Delta\mu/(2\mu_K^0)$ in the row $L_{2,3}$-$M_{2,3}$-$N_{2,3}$ edges, although the magnetic dichroism of quasicore states ($O_{2,3}$ and $N_{6,7}$ edges) became almost one order of magnitude larger as it was at the $L_{2,3}$ edges (compare Figs. 23 and 25). Besides, the lifetime widths of the core $O_{2,3}$ and $N_{6,7}$ levels are much smaller than the $L_{2,3}$ values [98]. The spectroscopy of Bi atoms in the ultrasoft x-ray energy range at the $O_{2,3}$ and $N_{6,7}$ edges may therefore be a useful tool for investigating the electronic and magnetic structure of MnBi.

Bi $M_{4,5}$ and $N_{4,5}$ spectra may be considered as an analog of the K spectrum to some extent. The K absorption spectrum
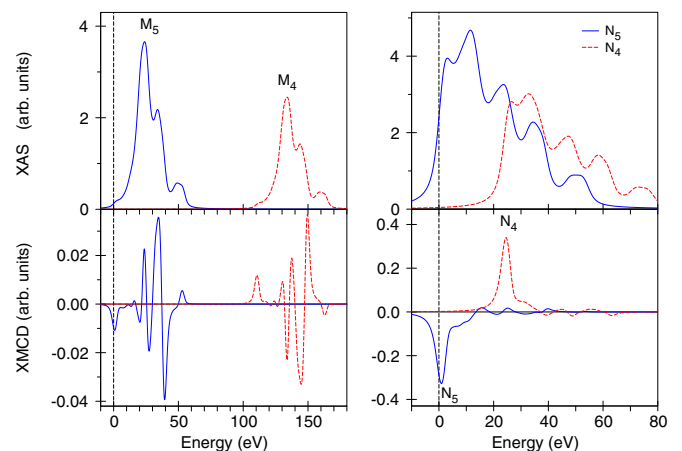

FIG. 24. (Color online) X-ray absorption (top panels) and XMCD spectra (lower panels) at the Bi $M_{4,5}$ (left panels) and edges $N_{4,5}$ (right panels) calculated using the LSDA+SO+U.
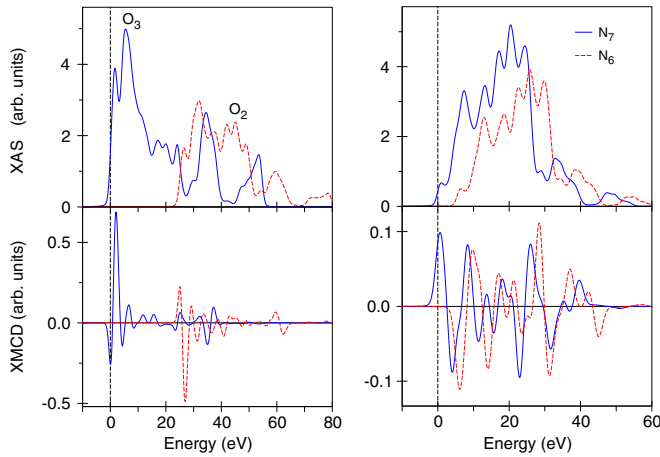
FIG. 25. (Color online) X-ray absorption (top panels) and XMCD (lower panels) spectra at the Bi $O_{2,3}$ (left panels) and $N_{6,7}$ (right panels) edges calculated in the LSDA+SO+U.

reflects the energy distribution of empty $p_{1/2}$ and $p_{3/2}$ energy states. The M_4 (N_4) absorption spectrum is due to the dipole selection rules occurring during the transition from the $3d_{3/2}$ ($4d_{3/2}$) core states to the $p_{1/2}$, $p_{3/2}$, and $f_{5/2}$ valence states above the Fermi level. The $p_{3/2}$, $f_{5/2}$, and $f_{7/2}$ states contribute to the M_5 (N_5) XASs. Results of the theoretical calculations of the circular dichroism in absorption at the $M_{4,5}$ and $N_{4,5}$ edges of MnBi are shown in Fig. 24.

It is interesting to compare the Bi XAS and XMCD spectra at the $L_{2,3}$, $O_{2,3}$, and $N_{6,7}$ edges. Due to the dipole selection rules, for unpolarized radiation (apart from the $s_{1/2}$ states which have a small contribution to the XAS) only the $3d_{3/2}$ states occur as final states for the L_2 as well as for the O_2 spectra. The L_3 and O_3 spectra reflect the energy distribution of both the $3d_{3/2}$ and $3d_{5/2}$ empty states. On the other hand, the N_7 absorption spectrum reflects only the $3d_{5/2}$ states (the density of the $g_{7/2,9/2}$ states is really very small), whereas for the N_6 XAS both the $3d_{3/2}$ and $3d_{5/2}$ states contribute. We therefore have an inverse situation: The N_6 absorption spectra correspond to the L_3 and O_3 spectra, and the N_7 is the analog of the L_2 and O_2 spectra. This situation is clearly seen in Figs. 25 and 23 where the theoretically calculated XMCD spectra of MnBi at the $O_{2,3}$, $N_{6,7}$, and $L_{2,3}$ edges is presented. The XMCD spectra at the L_3 edges are almost identical to the spectra at the N_6 edges. The XMCD spectra at the L_2 edges are also very similar to the spectra at the N_7 edges (but not identical because the energy distribution of the Bi $5d_{3/2}$ and $5d_{5/2}$ states is not exactly the same due to SO interaction). The spectral shape of the magnetic circular dichroism at the O_3 (O_2) edge also resembles the corresponding dichroism at the L_3 and N_6 (L_2 and N_7) edges. However, the intensity of the XMCD signal at the O_3 (O_2) edge is relatively larger near the edge. One can argue that at least for Bi the $L_{2,3}$ and $N_{6,7}$ spectra predominantly reflect atomic aspects of the valence bands. For the $O_{2,3}$ edges, the itinerant aspects are more important.

Because of the relatively small SO splitting of the $4f$ states of Bi (~ 3.0 eV), the N_6 and N_7 spectra have an appreciable overlap. For this reason, the N_7 spectrum contributes to some extent to the structure of the total $N_{6,7}$ spectrum in the region

of the N_6 edge (see Fig. 25). To decompose a corresponding experimental $N_{6,7}$ spectrum into its N_6 and N_7 parts will therefore be quite difficult in general. A similar problem also occurs in the XAS spectra at the O edge (see Fig. 25).

VI. CONCLUSIONS

We have performed relativistic LSDA+SO+U calculations of the electronic structure and Fermi surface properties in MnBi. It was found that the SO interaction and Coulomb correlations strongly affect the shape of the FS by changing the size and even the topology of some sheets of the FS in MnBi.

The x-ray absorption and x-ray magnetic dichroism of MnBi at the Mn K, $L_{2,3}$, and $M_{2,3}$ edges and the Bi $L_{2,3}$, $M_{2,3}$, $M_{4,5}$, $N_{2,3}$, $N_{4,5}$, $N_{6,7}$, and $O_{2,3}$ edges have been studied.

We showed that the SO coupling of Bi, the exchange splitting of Mn, and the Mn-Bi hybridization are all crucial components for a large MO Kerr effect in MnBi. It was determined that the main reason for a failure of previous LSDA calculations to describe the MO properties in MnBi is the significant underestimation of spin magnetic moment on the Mn atom. Two very different techniques (the LSDA+U method and an application of external magnetic field on the Mn atom) produce similar spin moment enhancement and consequently better MO and MAE values.

The LSDA+SO+U approach provides a proper value of magnetic moment on Mn atoms and correct easy magnetization direction for the entire temperature interval. The LSDA+SO+U theory produces MAE which is in very good quantitative agreement with experimental results in the 150–450 K temperature range. The physical reason for the observed spin reorientation is the unusual dependence of anisotropic Bi-Bi exchange on the in-plane lattice parameter or exchange striction mechanism.

It appears that the spin reorientation in MnBi correlates with the inversion of orbital moment minimum on Bi atom with temperature according to a Hund's rule. At lower temperature a maximum of orbital moment corresponds to a minimum of the total energy, while at room temperature it corresponds to the energy maximum.

For a large amount of properties that have been discussed in this paper, no prior theoretical or experimental studies have been performed. With high quality single crystal samples already available, the opportunity to perform the initial experimental study of many the properties discussed above becomes feasible and therefore our other theoretical predictions can be tested.

[1] J. Yang, K. Kamaraju, W. Yelon, and W. James, Appl. Phys. Lett. **79**, 1846 (2001).

[2] G. Q. Di, S. Iwata, S. Tsunashima, and S. Uchiyama, J. Magn. Magn. Mater. **104**, 1023 (1992).

[3] R. R. Heikes, Phys. Rev. **99**, 446 (1955).

[4] U. Rüdiger and G. Güntherodt, J. Appl. Phys. **88**, 4221 (2000).

[5] J. B. Yang, W. B. Yelon, W. J. James, Q. Cai, M. Kornecki, S. Roy, N. Ali, and P. I'Heritier, J. Phys.: Condens. Matter **14**, 6509 (2002).

[6] T. Chen and W. Stutius, IEEE Trans. Magn. **10**, 581 (1974).

[7] A. F. Andersen, W. Hälg, P. Fischer, and E. Stoll, Acta Chem. Scand. **21**, 1543 (1967).

[8] F. Heusler, Z. Angew. Chern. **17**, 260 (1904).

[9] E. Bekier, Int. Z. Metallogr. **7**, 83 (1914).

[10] N. Parravano and U. Perret, Gazz. Chim. Ital. **45**(1), 390 (1915).

[11] S. Hilpert and T. Dieckmann, Ber. Deut. Chern. Ges. **44**, 2831 (1911).

[12] U. Furst and F. Halla, Z. Physik Chern. B **40**, 285 (1938).

[13] E. Montignie, Bull. Soc. Chim. **5**, 343 (1938).

[14] F. Halla and E. Montignie, Z. Physik Chern. B **42**, 153 (1939).

[15] C. Guillaud, Ph.D. thesis, University of Strasbourg, Strasbourg, 1943.

[16] E. Adams, Rev. Mod. Phys. **25**, 306 (1953).

[17] T. Hihara and Y. Köi, J. Phys. Soc. Jpn. **29**, 343 (1970).

[18] W. E. Stutius, T. Chen, and T. R. Sandin, *Magnetism and Magnetic Materials*, AIP Conf. Proc. No. 18 (AIP, Melville, NY, 1974), p. 1222.

[19] H. J. Williams, R. C. Sherwood, F. G. Foster, and E. M. Keller, J. Appl. Phys. **28**, 1181 (1957).

[20] L. Mayer, J. Appl. Phys. **29**, 1003 (1958).

[21] L. Mayer, J. Appl. Phys. **31**, 3845 (1960).

[22] D. Chen, J. Appl. Phys. **42**, 3625 (1971).

[23] K. H. J. Buschow, in *Ferromagnetic Materials*, edited by E. P. Wohlfarth and K. H. J. Buschow (North-Holland, Amsterdam, 1988), Vol. 4, p. 588.

[24] D. Huang, X. W. Zheng, C. P. Luo, H. S. Yang, and Y. J. Wang, J. Appl. Phys. **75**, 6351 (1993).

[25] G. Q. Di and S. Uchiyama, Phys. Rev. B **53**, 3327 (1996).

[26] K. Harder, D. Menzel, T. Widmer, and J. Schoenes, J. Appl. Phys. **84**, 3625 (1998).

[27] R. Coehoorn and R. de Groot, J. Phys. F **15**, 2135 (1985).

[28] Z. W. Wang and M. C. Huang, Chin. Phys. Lett. **10**, 612 (1993).

[29] R. F. Sabiryanov and S. S. Jaswal, Phys. Rev. B **53**, 313 (1996).

[30] P. M. Oppeneer, V. N. Antonov, T. Kraft, H. Eschrig, A. N. Yaresko, and A. Y. Perlov, J. Appl. Phys. **80**, 1099 (1996).

[31] Yu. A. Uspenskii, E. T. Kulatov, and S. V. Halilov, Physica A **241**, 89 (1997).

[32] J. Köhler and J. Kübler, J. Phys.: Condens. Matter **8**, 8681 (1996).

[33] J. Köhler and J. Kübler, Physica B **402**, 237 (1997).

[34] L. V. Burkova, S. G. Ovchinnikov, V. A. Seredkin, and V. Y. Yakovchuk, J. Magn. Magn. Mater. **195**, 531 (1999).

[35] P. Ravindran, A. Delin, P. James, B. Johansson, J. M. Wills, R. Ahuja, and O. Eriksson, Phys. Rev. B **59**, 15680 (1999).

[36] M. Q. Tan, X. M. Tao, and S. N. Bao, Chin. Phys. **9**, 55 (2000).

[37] P. Mavropoulos, K. Sato, R. Zeller, P. H. Dederichs, V. Popescu, and H. Ebert, Phys. Rev. B **69**, 054424 (2004).

[38] J. C. Zheng and J. W. Davenport, Phys. Rev. B **69**, 144415 (2004).

[39] H. Weng, Y. Kawazoe, and J. Dong, Phys. Rev. B **74**, 085205 (2006).

[40] M. Li, T. Ariizumi, K. Koyanagi, and S. Suzuki, Jpn. J. Appl. Phys. **46**, 3455 (2007).

[41] B. Sanyal and O. Eriksson, J. Appl. Phys. **103**, 07D704 (2008).

[42] L. Kahal and M. Ferhat, J. Appl. Phys. **107**, 043910 (2010).

[43] J. N. Goncalves, V. S. Amaral, J. G. Correia, and A. M. L. Lopes, Phys. Rev. B **83**, 104421 (2011).

[44] P. Kharel, P. Thapa, P. Lukashev, R. F. Sabirianov, E. Y. Tsymbal, D. J. Sellmyer, and B. Nadgorny, Phys. Rev. B **83**, 024415 (2011).

[45] P. R. Bandaru, T. D. Sands, Y. Kubota, and E. E. Marinero, Appl. Phys. Lett. **72**, 2337 (1998).

[46] J. Schoenes, in *Electronic and Magnetic Properties of Metals and Ceramics*, edited by R. W. Cahn, P. Haasen, and E. J. Kramer, Materials Science and Technology Vol. 3A (Verlag Chemie, Weinheim, 1992), p. 147.

[47] R. Kubo, J. Phys. Soc. Jpn. **12**, 570 (1957).

[48] C. S. Wang and J. Callaway, Phys. Rev. B **9**, 4897 (1974).

[49] V. N. Antonov, A. I. Bagljuk, A. Y. Perlov, V. V. Nemoshkalenko, V. N. Antonov, O. K. Andersen, and O. Jepsen, Low Temp. Phys. **19**, 494 (1993).

[50] V. Antonov, B. Harmon, and A. Yaresko, *Electronic Structure and Magneto-Optical Properties of Solids* (Kluwer, Dordrecht, 2004).

[51] J. Kunes and P. M. Oppeneer, Phys. Rev. B **67**, 024431 (2003).

[52] J. Smith and H. P. J. Wjin, *Ferrites* (Philips Technical Library, Eindhoven, 1959).

[53] V. N. Antonov, A. Y. Perlov, A. P. Shpak, and A. N. Yaresko, J. Magn. Magn. Mater. **146**, 205 (1995).

[54] O. K. Andersen, Phys. Rev. B **12**, 3060 (1975).

[55] I. V. Solovyev, A. I. Liechtenstein, V. A. Gubanov, V. P. Antropov, and O. K. Andersen, Phys. Rev. B **43**, 14414 (1991).

[56] P. E. Blöchl, O. Jepsen, and O. K. Andersen, Phys. Rev. B **49**, 16223 (1994).

[57] J. P. Perdew and A. Zunger, Phys. Rev. B **23**, 5048 (1981).

[58] V. I. Anisimov, J. Zaanen, and O. K. Andersen, Phys. Rev. B **44**, 943 (1991).

[59] L. Hedin, Phys. Rev. **139**, A796 (1965).

[60] N. E. Zein and V. P. Antropov, Phys. Rev. Lett. **89**, 126402 (2002).

[61] W. Metzner and D. Vollhardt, Phys. Rev. Lett. **62**, 324 (1989).

[62] A. Georges, G. Kotliar, W. Krauth, and M. J. Rozenberg, Rev. Mod. Phys. **68**, 13 (1996).

[63] A. N. Yaresko, V. N. Antonov, and P. Fulde, Phys. Rev. B **67**, 155103 (2003).

[64] O. Bengone, M. Alouani, P. Blöchl, and J. Hugel, Phys. Rev. B **62**, 16392 (2000).

[65] V. I. Anisimov and O. Gunnarsson, Phys. Rev. B **43**, 7570 (1991).

[66] I. V. Solovyev, P. H. Dederichs, and V. I. Anisimov, Phys. Rev. B **50**, 16861 (1994).

[67] P. H. Dederichs, S. Blügel, R. Zeller, and H. Akai, Phys. Rev. Lett. **53**, 2512 (1984).

[68] W. E. Pickett, S. C. Erwin, and E. C. Ethridge, Phys. Rev. B **58**, 1201 (1998).

[69] M. Cococcioni and S. de Gironcoli, Phys. Rev. B **71**, 035105 (2005).

[70] K. Nakamura, R. Arita, Y. Yoshimoto, and S. Tsuneyuki, Phys. Rev. B **74**, 235113 (2006).

[71] F. Aryasetiawan, K. Karlsson, O. Jepsen, and U. Schonberger, Phys. Rev. B **74**, 125106 (2006).

[72] E. Antonides, E. C. Janse, and G. A. Sawatzky, Phys. Rev. B **15**, 1669 (1977).

[73] D. van der Marel, G. A. Sawatzky, and F. U. Hillebrecht, Phys. Rev. Lett. **53**, 206 (1984).

[74] M. Springer and F. Aryasetiawan, Phys. Rev. B **57**, 4364 (1998).

[75] T. Kotani, J. Phys.: Condens. Matter **12**, 2413 (2000).

[76] F. Aryasetiawan, M. Imada, A. Georges, G. Kotliar, S. Biermann, and A. I. Lichtenstein, Phys. Rev. B **70**, 195104 (2004).

[77] I. V. Solovyev and M. Imada, Phys. Rev. B **71**, 045103 (2005).

[78] T. Miyake, F. Aryasetiawan, and M. Imada, Phys. Rev. B **80**, 155134 (2009).

[79] T. Miyake and F. Aryasetiawan, Phys. Rev. B **77**, 085122 (2008).

[80] K. Nakamura, R. Arita, and M. Imada, J. Phys. Soc. Jpn. **77**, 093711 (2008).

[81] T. Miyake, L. Pourovskii, V. Vildosola, S. Biermann, and A. Georges, J. Phys. Soc. Jpn. **77**, 99 (2008).

[82] T. Miyake, F. Aryasetiawan, and M. Imada, Phys. Rev. B **80**, 155134 (2009).

[83] A. V. Postnikov and V. P. Antropov, Comp. Mat. Sci. **17**, 438 (2000).

[84] L. Zhiqiang, L. Helie, L. Wuyan, Z. Zhi, and Z. Qingqi, Solid State Commun. **79**, 791 (1991).

[85] J. B. Yang, Y. B. Yang, X. G. Chen, X. B. Ma, J. Z. Han, Y. C. Yang, S. Guo, A. R. Yan, Q. Z. Huang, M. M. Wu *et al.*, Appl. Phys. Lett. **99**, 082505 (2011).

[86] K. Koyama, Y. Mitsui, and K. Watanabe, Sci. Technol. Adv. Mater. **9**, 024204 (2008).

[87] N. Vast, B. Siberchicot, and P. G. Zerah, J. Phys.: Condens. Matter **4**, 10469 (1992).

[88] J. C. Slonczewski, Phys. Rev. **110**, 1341 (1958).

[89] R. L. Streever, Phys. Rev. B **19**, 2704 (1979).

[90] K. Yosida, A. Okiji, and S. Chikazumi, Prog. Theor. Phys. **33**, 559 (1965).

[91] M. Cinal, D. M. Edwards, and J. Mathon, Phys. Rev. B **50**, 3754 (1994).

[92] V. P. Antropov, L. Ke, and D. Aberg, Solid State Commun. **194**, 35 (2014).

[93] L. Ke, K. D. Belashchenko, M. van Schilfgaarde, T. Kotani, and V. P. Antropov, Phys. Rev. B **88**, 024404 (2013).

[94] M. Montalti, A. Credi, L. Prodi, and M. T. Gandolfi, in *Handbook of Photochemistry*, edited by N. J. Turro (Taylor & Francis, Boca Raton, FL, 2006), p. 629.

[95] N. A. Zarkevich, L.-L. Wang, and D. D. Johnson, APL Mat. **2**, 032103 (2014).

[96] W. Reim and J. Schoenes, in *Ferromagnetic Materials*, edited by E. P. Wohlfarth and K. H. J. Buschow (North-Holland, Amsterdam, 1990), Vol. 5, p. 133.

[97] L. Uba, S. Uba, V. N. Antonov, A. N. Yaresko, T. Slezak, and J. Korecki, Phys. Rev. B **62**, 13731 (2000).

[98] J. C. Fuggle and J. E. Inglesfield, *Unoccupied Electronic States*, Topics in Applied Physics Vol. 69 (Springer, New York, 1992).